J. Fluid Mech. (2009), *vol.* 620, *pp.* 263–298. © 2009 Cambridge University Press
doi:10.1017/S0022112008004394 Printed in the United Kingdom

Input–output analysis, model reduction and control of the flat-plate boundary layer

SHERVIN BAGHERI, LUCA BRANDT AND DAN S. HENNINGSON†

Linné Flow Centre, KTH Mechanics, SE-100 44 Stockholm, Sweden

(Received 12 May 2008 and in revised form 22 September 2008)

The dynamics and control of two-dimensional disturbances in the spatially evolving boundary layer on a flat plate are investigated from an input–output viewpoint. A set-up of spatially localized inputs (external disturbances and actuators) and outputs (objective functions and sensors) is introduced for the control design of convectively unstable flow configurations. From the linearized Navier–Stokes equations with the inputs and outputs, controllable, observable and balanced modes are extracted using the snapshot method. A balanced reduced-order model (ROM) is constructed and shown to capture the input–output behaviour of the linearized Navier–Stokes equations. This model is finally used to design a $\mathscr{H}_2$-feedback controller to suppress the growth of two-dimensional perturbations inside the boundary layer.

1. Introduction

Many powerful linear systems and control theoretical tools have been out of reach for the fluid mechanics community due to the complexity of the Navier–Stokes equations. Two elements that have enabled a systematic approach to flow control are the availability of increasingly powerful computer resources and the recent advances of matrix-free methods. In this paper, the linearized Navier–Stokes equations including inputs and outputs are analysed using systematic tools from linear systems and control theory. The techniques do not rely on physical insight into the specific flow configuration and can in principle be applied to any geometry.

We will focus on the flat-plate geometry, which still poses a computational challenge. The two-dimensional Blasius boundary layer is non-parallel, i.e. spatially evolving, and therefore has two inhomogeneous spatial directions. Many tools in both stability analysis and control theory rely on the linearized stability operator, which even for two-dimensional flows becomes very large when discretized. As an example, a moderate grid resolution with 200 points in two directions leads to a system matrix with a memory demand of 10 gigabytes, whereas storing a flow field requires only 3 megabytes. It is therefore essential to either approximate or develop algorithms in which large matrices are avoided, and the storage demands are of the order of few flow fields. Matrix-free methods employ the 'timestepper approach' in which, given a flow field, a Navier–Stokes code is used to provide a field at a later time. The timestepper technique has become increasingly popular in stability analysis, for both computing the largest transient growth (Blackburn, Barkley & Sherwin 2008) and performing asymptotic analysis (Barkley, Gomes & Henderson 2002). Another example of a

† Email address for correspondence: henning@mech.kth.se

https://doi.org/10.1017/S0022112008004394 Published online by Cambridge University Press

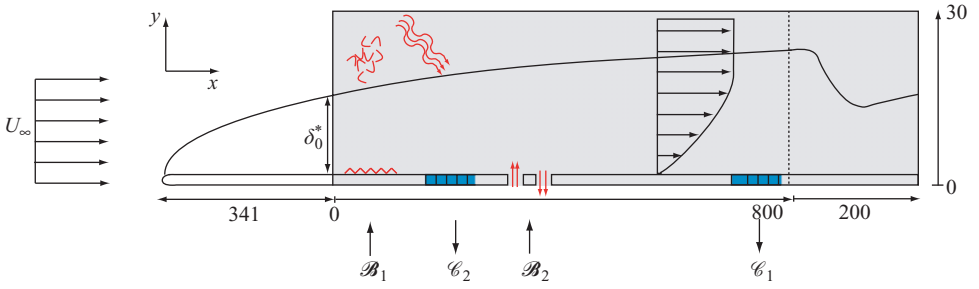


FIGURE 1. Conceptual figure of the input–output configuration used for the control of perturbations in a two-dimensional flat-plate geometry. The computational domain $\Omega = (0, L_x) \times (0, L_y)$, shown by the grey region, extends from $x = 0$ to $x = 1000$ with the fringe region starting at $x = 800$. The first input $\mathscr{B}_1$, located at $(x_w, y_w) = (35, 1)$, models the initial receptivity phase, where disturbances are induced by free stream turbulence, acoustic waves or wall roughness. The actuator $\mathscr{B}_2$ provides a means to manipulate the flow, in this case by a localized volume forcing, and is centred at $(x_u, y_u) = (400, 1)$. Two sensors $\mathscr{C}_1$ and $\mathscr{C}_2$ are located at $(x_v, y_v) = (300, 1)$ and $(x_z, y_z) = (750, 1)$ respectively. The upstream measurements are used to estimate the incoming perturbations, while the downstream sensor quantifies the effect of the control. Note that in this work all the inputs and outputs are Gaussian functions given by (2.14).

matrix-free method is the snapshot method introduced by Sirovich (1987), which allows the proper orthogonal decomposition (POD) of flow fields without solving large eigenvalue problems.

The starting point of modern optimal and robust control design, also denoted as $\mathscr{H}_2$- and $\mathscr{H}_\infty$-control, is an input–output formulation referred to as the standard state-space formulation (Zhou, Salomon & Wu 1999). The well-known stochastic approach to optimal control referred to as linear quadratic Gaussian (LQG) is an example of an $\mathscr{H}_2$ controller. In this work, we consider three inputs and two outputs; the inputs represent external disturbances, measurement noise and the actuator, whereas the outputs represent measurements for estimation and of the objective functional to be minimized (see figure 1). The control problem is to supply the actuator with an optimal signal based on the measurements taken from the first sensor, such that the effect of external disturbances and measurement noise on the disturbance energy is minimized at the location of the second sensor. Given the physical distribution of the inputs and outputs, the control design process amounts to the determination of input signals when output signals are given. Therefore, for successful control design it is sufficient to capture only a fraction of the dynamics, namely the relationships between input and output signals.

The aim of this study is to build a model of low dimension that captures the input–output behaviour of the flat-plate boundary layer and use this model for optimal feedback control design. With the help of the adjoint Navier–Stokes equations two fundamental dynamical structures are identified: (i) the flow structures that are influenced by the inputs; (ii) the flow structures that the outputs are sensitive to. These controllable and observable structures determine the input–output behaviour completely for linear systems. It is well known in systems theory that these two sets of modes can be balanced and represented by one set of modes, called the balanced modes. In this way, the flow structures that capture most of the input–output behaviour are extracted and used as the projection basis for model reduction. The method employed in this work to compute the balanced modes is called

https://doi.org/10.1017/S0022112008004394 Published online by Cambridge University Press

snapshot-based balanced truncation (Willcox & Peraire 2002; Rowley 2005). This method has been applied to the channel flow (Ilak & Rowley 2008) and the flow around a pitching airfoil (Ahuja *et al.* 2007). Unlike previous work, we do not combine the snapshot-based balanced truncation with an output projection approach in order to describe the flow dynamics. Our control design and performance evaluation is based on input and output signals rather than on the space–time evolution of the entire flow.

Previous work in flow control involving model reduction and control design has typically relied on physical insight into the specific flow situation rather than a systematic approach detached from the application (see Kim & Bewley 2007, for a recent review). For parallel flows, for instance it is possible to decouple the linear equations in Fourier space. Control, estimation and other types of optimization can then be performed independently for each wavenumber and transformed back to physical space. This approach has been adopted for channel flow in Högberg, Bewley & Henningson (2003) and even extended to weakly nonparallel flows by Chevalier *et al.* (2007*a*). Another example is the projection of the linearized Navier–Stokes equations on a set of modes such as global eigenmodes of the stability operator or POD modes. Although these methods have been applied with considerable success to various flows (Gillies 1998; Åkervik *et al.* 2007) their success is strongly dependent on the dynamics of the specific flow situation. For many open shear flows the global eigenmodes and their associated adjoint modes can become widely separated in the streamwise direction (Chomaz 2005) and gradually move away from the locations of the inputs and outputs (Lauga & Bewley 2003). As a consequence controllability and observability of the global eigenmodes is gradually diminished. If controllability/observability is lost for any unstable eigenmode, no control scheme will be able to stabilize the system. The POD basis also has limitations for describing the input–output behaviour. Although it is optimal for capturing the energy of the response to an input, it does not always capture the input itself and takes no consideration of the output. However, examples of successful adaptations of POD modes can be found in Noack *et al.* (2003) and Siegel *et al.* (2008) for the globally unstable flow past a circular cylinder.

The paper is organized as follows: We start with describing the flow domain, the inputs, the outputs and the control problem in § 2. In this section the mathematical framework is presented with evolution, controllability and observability operators and their associated adjoint operators. These operators are used to introduce the Gramians and balanced modes in § 3, where we also investigate the input–output behaviour of our linear system and discuss the controllable, observable and balanced modes. In § 4 the impulse and harmonic response of the balanced reduced-order model (ROM) are compared to the full Navier–Stokes equations, and the model reduction error is quantified. Section 5 deals with the control design. We briefly introduce the $\mathscr{H}_2$ framework and evaluate the closed-loop performance. Concluding remarks and a summary of the presented material are offered in the last section. Finally, in the appendices we derive the adjoint operators and describe the snapshot method, the solution of the $\mathscr{H}_2$ problem and our timestepper.

2. Problem formulation

2.1. *Governing equations*

We consider the linear spatio-temporal evolution of two-dimensional disturbances in a viscous, incompressible flow over a flat plate. The geometry of the problem and the physical domain $\Omega = (0, L_x) \times (0, L_y)$ are shown in figure 1. The disturbance

https://doi.org/10.1017/S0022112008004394 Published online by Cambridge University Press

behaviour is governed by the Navier–Stokes equations linearized about a spatially evolving zero-pressure-gradient boundary layer:

$$\frac{\partial \boldsymbol{u}}{\partial t} = -(\boldsymbol{U}\cdot\nabla)\boldsymbol{u} - (\boldsymbol{u}\cdot\nabla)\boldsymbol{U} - \nabla p + Re^{-1}\nabla^2\boldsymbol{u} + \lambda(x)\boldsymbol{u}, \tag{2.1a}$$

$$0 = \nabla\cdot\boldsymbol{u}, \tag{2.1b}$$

$$\boldsymbol{u} = \boldsymbol{u}_0 \qquad \text{at} \quad t = 0. \tag{2.1c}$$

The disturbance velocity and pressure field at position $\boldsymbol{x} = (x, y)$ and time t are represented by $\boldsymbol{u}(\boldsymbol{x}, t) = (u, v)^T$ and $p(\boldsymbol{x}, t)$, respectively. The divergence operator is denoted by $\nabla = (\partial_x, \partial_y)^T$. The Reynolds number is defined as $Re = U_\infty \delta_0^*/\nu$, where U_∞ is the free stream velocity and δ_0^* the displacement thickness at the computational inflow $x_0 = 0$. All the simulations were performed at $Re = 1000$ which corresponds to a distance of $341\delta_0^*$ from the leading edge to the inlet of the computational domain. The base flow $\boldsymbol{U} = (U, V)^T(x, y)$ is a solution to the steady, nonlinear Navier–Stokes equations.

The term $\lambda(x)$ is used to enforce periodicity of the physical flow in the streamwise direction, so that a spectral Fourier expansion technique can be employed for our numerical solution. This function is non-zero only in a fringe region at the end of the domain (see figure 1) in which it forces the outgoing perturbation amplitude to zero (see Appendix C and Nordström Nordin & Henningson 1999 for further details). As discussed in Åkervik *et al.* (2008) the growth rate of individual eigenvalues in the spectrum of the linearized Navier–Stokes equations depends on the outflow boundary conditions. However, the perturbation dynamics remain unaltered for different boundary conditions, including the fringe method.

The solutions to (2.1) satisfy no-slip condition at the plate and vanish at the upper boundary $L_y = 30\delta_0^*$ which is chosen to be well outside the boundary layer. The boundary conditions hence are

$$\boldsymbol{u}(0, y) = \boldsymbol{u}(L_x, y), \tag{2.2a}$$

$$\boldsymbol{u}(x, 0) = \boldsymbol{u}(x, L_y) = 0. \tag{2.2b}$$

2.2. *Standard state-space formulation and the $\mathscr{H}_2$ problem*

The Navier–Stokes equations may be written in the 'standard state-space form' (Zhou, Doyle & Glover 2002) useful for applying tools from systems theory and for $\mathscr{H}_2/\mathscr{H}_\infty$ control design.

In the state-space framework, any divergence-free, smooth disturbance field $\boldsymbol{u}(\boldsymbol{x})$ that satisfies the boundary conditions (2.2) is an element of the (Hilbert) state space

$$\mathbb{X} = \{\boldsymbol{u}(\boldsymbol{x}) \in L^2(\Omega) \mid \nabla\cdot\boldsymbol{u}(\boldsymbol{x}) = 0,\ \boldsymbol{u}(0, y) = \boldsymbol{u}(L_x, y),\ \boldsymbol{u}(x, 0) = \boldsymbol{u}(x, L_y) = 0\}. \tag{2.3}$$

A state is a velocity field $\boldsymbol{u}(\boldsymbol{x}, t)$ at time t or equivalently a point on a trajectory in $\mathbb{X}$. Let us introduce a bounded linear solution operator $\mathscr{T}(t) : \mathbb{X} \to \mathbb{X}$ for the state variable $\boldsymbol{u}$ as

$$\boldsymbol{u}(\boldsymbol{x}, t + s) = \mathscr{T}(t)\boldsymbol{u}(\boldsymbol{x}, s). \tag{2.4}$$

Given a perturbation field at time s, $\mathscr{T}(t)$ provides the velocity field at a later time $t + s$ by solving (2.1) with $\boldsymbol{u}_0 = \boldsymbol{u}(\boldsymbol{x}, s)$ and (2.2). The operator satisfies the properties $\mathscr{T}(t + s) = \mathscr{T}(t)\mathscr{T}(s)$, $\mathscr{T}(0) = I$ and can be considered a semi-group (see, e.g. Pazy

https://doi.org/10.1017/S0022112008004394 Published online by Cambridge University Press

1983; Trefethen & Embree 2005) of the form $\exp(\mathscr{A}t)$† with the infinitesimal generator

$$\mathscr{A}\boldsymbol{u} = \lim_{\delta t \to 0} \frac{\mathscr{T}(\delta t)\boldsymbol{u} - \boldsymbol{u}}{\delta t}. \tag{2.5}$$

The linearized Navier–Stokes equations (2.1) with boundary conditions (2.2) can be cast as an initial-value problem in state-space form

$$\dot{\boldsymbol{u}} = \mathscr{A}\boldsymbol{u}, \tag{2.6}$$

$$\boldsymbol{u} = \boldsymbol{u}_0 \qquad \text{at} \quad t = 0. \tag{2.7}$$

Note that the action of $\mathscr{A}$ on $\boldsymbol{u}$ corresponds to evaluating the right-hand side of the Navier–Stokes equations and enforcing the boundary conditions. The pressure term can be obtained from the velocity field by solving a Poisson equation (Kreiss, Lundbladh & Henningson 1993). Alternatively, the state-space form can be obtained by defining a projection operator that projects the equations onto $\mathbb{X}$ (Chorin & Marsden 1990; Bewley, Temam & Ziane 2000).

In this work, the action of the operator $\mathscr{A}$ is approximated numerically: $\mathscr{T}(t)\boldsymbol{u}(\boldsymbol{x}, s)$ is obtained by solving the partial differential equation (2.1) using a timestepper, i.e. a Navier–Stokes solver (Barkley *et al.* 2002), with $\boldsymbol{u}(\boldsymbol{x}, s)$ as initial condition. In its simplest form, a timestepper sets up a grid in space and time and computes approximate solutions on this grid by marching in time. This approach is computationally feasible also for very large systems, since matrices are not stored. The timestepper used and the corresponding numerical method are described in Appendix C.

We introduce the forcing $\boldsymbol{f}(\boldsymbol{x}, t)$, which is also referred to as the input. The forcing $\boldsymbol{f}$ is decomposed into external disturbances $\mathscr{B}_1 w$ and a control $\mathscr{B}_2 u$, i.e.

$$\boldsymbol{f} = \mathscr{B}_1 w + \mathscr{B}_2 u, \tag{2.8}$$

where the input signals $w(t)$, $u(t)$ are functions of time and $\mathscr{B}_1, \mathscr{B}_2$ are bounded linear mappings from $\mathbb{R} \to \mathbb{X}$. The first mapping, $\mathscr{B}_1$, represents the spatial distribution of the sources of external disturbances acting on the flow (see figure 1). In our model, the input forcing $\mathscr{B}_1$ is located at the upstream end of the domain to model the upstream receptivity phase, when disturbances are introduced into the boundary layer by, e.g. roughness and free stream perturbations. The actuator used for control is defined by the mapping $\mathscr{B}_2$, which represents a localized volume force, mimicking blowing and suction at the wall. Finally, $u(t)$ represents the control signal we wish to apply and is based on the sensor measurements.

Information about the disturbance behaviour is given by two outputs:

$$z = \mathscr{C}_1 \boldsymbol{u} + l u, \tag{2.9}$$

$$v = \mathscr{C}_2 \boldsymbol{u} + \alpha g, \tag{2.10}$$

where the output signals z, v are functions of time and $\mathscr{C}_1, \mathscr{C}_2$ are bounded linear functionals from $\mathbb{X} \to \mathbb{R}$. The sensor defined by $\mathscr{C}_1$ is located far downstream, and it is used to evaluate the level of the disturbance amplitude. Therefore it reveals whether the 'objective' of our control has been met. In particular, the objective is to find a control signal $u(t)$ such that the perturbation energy in the flow is minimized downstream at the location defined by $\mathscr{C}_1$. To design an efficient controller, however,

† This is only true if $\mathscr{A}$ is a bounded operator. In general, for a closed operator $\mathscr{A}$ with a dense domain, the relation between $\mathscr{T}$ and $\mathscr{A}$ is $\mathscr{T}(t)\boldsymbol{u} = \lim_{n\to\infty}(I - t/n\mathscr{A})^{-n}\boldsymbol{u}$ (see, e.g. Pazy 1983).

https://doi.org/10.1017/S0022112008004394 Published online by Cambridge University Press

the energy input expended in the actuation should be limited; thus, the control effort is penalized with a scalar l. For large values of l the control effort is considered to be expensive, whereas small values indicate cheap control. This results in an objective functional of the form

$$\|z\| = \|\mathscr{C}_1 \boldsymbol{u}\| + l\|u\| \tag{2.11}$$

and explains why the control signal is added to the sensor signal when defining the output signal z. The norms in (2.11) are associated with the inner products defined in the next section. In the definition of z we have assumed $\langle lu, \mathscr{C}_1 \boldsymbol{u}\rangle = 0$, so that there is no cross-weighting between the flow energy and control input (Zhou *et al.* 1999).

The second output signal $v(t)$ is the measurement signal extracted from the sensor $\mathscr{C}_2$. This signal is the only information delivered to the controller in order to provide a control signal such that the above objective is met. The additional term $g(t)$ accounts for noise contaminating the measurements. This term can be considered as a third forcing, but rather than forcing the Navier–Stokes equations it forces the measurements. Large values of the scalar α indicate high level of noise corruption in the output signal, whereas for low values of α the measurement v reflects information about the flow field with high fidelity.

The choice of the relative position of the sensor $\mathscr{C}_2$ and actuator $\mathscr{B}_2$ used in the control design process and reported in figure 1 is based on the knowledge of the behaviour of boundary layer instabilities. For convectively unstable flows, disturbances eventually leave the control domain; therefore there exists only a window of opportunity in time to reduce the growth of these disturbances, while they are convected downstream. As a consequence, the sensor placement in the streamwise direction is a trade-off. For a good estimation performance it should be placed downstream, so that the disturbance energy has amplified, but for a good controller performance, it should be placed upstream to provide the actuator an estimate of the flow dynamics as soon as possible. Similarly, there is a trade-off when choosing the location of the actuator, since its effects on the disturbance behaviour is limited to the nearby region. It is rather inefficient to place it either far downstream, where the disturbances have already experienced a substantial growth, or far upstream, where the disturbances will again have the opportunity to grow.

A completely different choice of sensor and actuator placement is appropriate in the case of globally unstable flows (see Bagheri *et al.* 2008), when the whole flow beats at a specific frequency. Since the disturbances never leave the laboratory frame, one can place the measurement sensor at the place at which the disturbance energy is the largest and the actuator at the place at which the sensitivity of the disturbances to forcing is the largest. In many open shear flows these locations are, respectively, far downstream, where the global eigenmodes of the linearized operator are located, and far upstream, where the adjoint global eigenmodes reveal high flow sensitivity. See, for example Åkervik *et al.* (2007) for the case in which feedback control applied to flow separation over a long shallow cavity.

The Navier–Stokes equations (2.1) with input vector $\boldsymbol{f} = (w, g, u)^T$ as an element in the input space $\mathbb{U} = \mathbb{R}^3$ and output vector $\boldsymbol{y} = (z, v)^T$ as an element in the output space $\mathbb{Y} = \mathbb{R}^2$ may now be written in the standard state-space form

$$\dot{\boldsymbol{u}} = \mathscr{A}\boldsymbol{u} + \mathscr{B}\boldsymbol{f}, \tag{2.12a}$$

$$\boldsymbol{y} = \mathscr{C}\boldsymbol{u} + \mathscr{D}\boldsymbol{f}, \tag{2.12b}$$

$$\boldsymbol{u} = \boldsymbol{u}_0 \qquad \text{at} \quad t = 0, \tag{2.12c}$$

https://doi.org/10.1017/S0022112008004394 Published online by Cambridge University Press

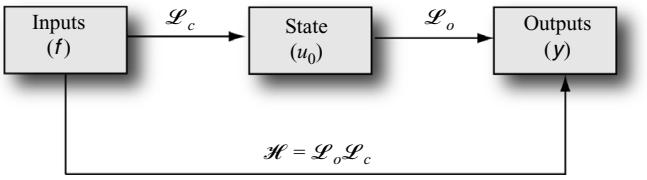


FIGURE 2. The operators used to examine the system input-output behaviour. The controllability operator $\mathscr{L}_c$ relates past inputs to the present state, while the observability mapping $\mathscr{L}_o$ relates the present state to the future outputs. Their combined action is expressed by the Hankel operator $\mathscr{H}$.

where $\mathscr{A}$ has been defined in (2.5). Furthermore, we have $\mathscr{C} = (\mathscr{C}_1, \mathscr{C}_2)^T$, $\mathscr{B} = (\mathscr{B}_1, 0, \mathscr{B}_2)$ and

$$\mathscr{D} = \begin{pmatrix} 0 & 0 & l \\ 0 & \alpha & 0 \end{pmatrix}. \tag{2.13}$$

The system (2.12) is asymptotically stable; i.e. in the global framework all the eigenmodes of the linearized Navier–Stokes system for a spatial boundary layer represent perturbations decaying in time.

Finally, we define the spatial distribution of the sensors and actuators introduced above. Here, the input and output operators are modelled with the Gaussian function $h(\boldsymbol{x}, \boldsymbol{x}_0)$, defined as

$$\boldsymbol{h}(\boldsymbol{x}; \boldsymbol{x}_0) = \begin{pmatrix} \sigma_x \gamma_y \\ -\sigma_y \gamma_x \end{pmatrix} \exp\left(-\gamma_x^2 - \gamma_y^2\right), \tag{2.14}$$

where

$$\gamma_x = \frac{x - x_0}{\sigma_x}, \qquad \gamma_y = \frac{y - y_0}{\sigma_y}. \tag{2.15}$$

The scalar quantities $\sigma_x = 4$, $\sigma_y = 1/4$ and x_0, y_0 (the latter two being given in the caption of figure 1) determine, respectively, the size and location of the inputs and outputs. They are all of the same size but located at different streamwise locations, as shown schematically in figure 1. With these definitions we have

$$\mathscr{B} = (\boldsymbol{h}(\boldsymbol{x}; \boldsymbol{x}_w), 0, \boldsymbol{h}(\boldsymbol{x}; \boldsymbol{x}_u)) \tag{2.16}$$

and

$$\mathscr{C}\boldsymbol{u} = \int_\Omega \begin{pmatrix} \boldsymbol{h}(\boldsymbol{x}; \boldsymbol{x}_z)^T \boldsymbol{u} \\ \boldsymbol{h}(\boldsymbol{x}; \boldsymbol{x}_v)^T \boldsymbol{u} \end{pmatrix} \mathrm{d}x\, \mathrm{d}y. \tag{2.17}$$

The particular shape of sensor and actuators implies that the inputs amount to localized volume forcing, whereas the flow measurements are obtained by averaging the velocity field over small domains, using the Gaussian function as weights.

2.3. *Controllability and observability operators*

When performing model reduction for control design, one wishes to retain the relationship between the inputs and the outputs in the low-order system. Following linear systems theory, the properties of the input-output system (2.12) can be described by the two operators introduced in this section. In the framework presented next we assume that sufficient regularity exists, so that all operators are bounded in the chosen metrics. See figure 2 and table 1 for an overview of the operators.

https://doi.org/10.1017/S0022112008004394 Published online by Cambridge University Press

Operator	Mapping	Definition	Adjoint operator
Evolution	$\mathbb{X} \to \mathbb{X}$	$\mathscr{T}(t)\boldsymbol{u}(s) = \boldsymbol{u}(t+s)$	$\mathscr{T}^*(t)\boldsymbol{u}(s) = \boldsymbol{u}(s-t)$
Controllability	$\mathbb{U}((-\infty, 0]) \to \mathbb{X}$	$\mathscr{L}_c\boldsymbol{f}(t) = \int_{-\infty}^{0} \mathscr{T}(-t)\mathscr{B}\boldsymbol{f}(t)\,\mathrm{d}t$	$\mathscr{L}_c^*\boldsymbol{u}_0 = \mathscr{B}^*\mathscr{T}^*(-t)\boldsymbol{u}_0$
Observability	$\mathbb{X} \to \mathbb{Y}([0, \infty))$	$\mathscr{L}_o(t)\boldsymbol{u}_0 = \mathscr{C}\mathscr{T}(t)\boldsymbol{u}_0$	$\mathscr{L}_o^*(t)\boldsymbol{f} = \int_0^{\infty} \mathscr{T}^*(t)\mathscr{C}^*\boldsymbol{f}\,\mathrm{d}t$
Hankel	$\mathbb{U}((-\infty, 0]) \to \mathbb{Y}([0, \infty))$	$\boldsymbol{y} = \mathscr{L}_o(t)\mathscr{L}_c\boldsymbol{f}$	$\boldsymbol{f} = \mathscr{L}_c^*(t)\mathscr{L}_o^*\boldsymbol{y}$

TABLE 1. The linear operators used in this work. See Appendix A for further details and derivations of the adjoint operators.

The operators needed to describe the input–output behaviour can be related to the formal solution of the system of (2.12), which is

$$\boldsymbol{y}(t) = \mathscr{C}\mathscr{T}(t)\boldsymbol{u}_0 + \mathscr{C}\int_0^t \mathscr{T}(t-\tau)\mathscr{B}\boldsymbol{f}(\tau)\,\mathrm{d}\tau + \mathscr{D}\boldsymbol{f}(t). \tag{2.18}$$

In this expression, we identify the first term on the right-hand side with the homogeneous solution and the second term with the particular solution stemming from the forcing $\boldsymbol{f}$. Note that in our case the forcing term $\mathscr{B}$ is an element in $\mathbb{X}$; i.e. it is divergence-free and satisfies the boundary conditions. For a more general forcing $\boldsymbol{f}$, only the divergence-free part of the forcing $\hat{\boldsymbol{f}}$ will affect the output signal. The difference $\hat{\boldsymbol{f}} - \boldsymbol{f}$ can be written as the gradient of a scalar and thus will only modify the pressure (Bewley *et al.* 2000). The third part of (2.18) relates the input to the output through the matrix $\mathscr{D}$ without any operators involved. Without loss of generality, we will neglect this term for now and consider it again in § 5 for control design.

In systems theory, the quantitative investigation of the input-output properties of a linear system is commonly performed through the mappings sketched in figure 2. We begin by introducing the controllability operator $\mathscr{L}_c : \mathbb{U}((-\infty, 0]) \to \mathbb{X}$:

$$\boldsymbol{u}_0 = \mathscr{L}_c\boldsymbol{f}(t) = \int_{-\infty}^{0} \mathscr{T}(-\tau)\mathscr{B}\boldsymbol{f}(\tau)\,\mathrm{d}\tau. \tag{2.19}$$

This operator describes the mapping of any input $\boldsymbol{f}(t)$ with $t \in (-\infty, 0]$ onto the state vector $\boldsymbol{u}$ at the reference time $t = 0$. The input space $\mathbb{U}((-\infty, 0])$ contains input trajectories in the past time $t \in (-\infty, 0]$. The associated inner product is given in § A.1 of Appendix A. The action of $\mathscr{L}_c$ can be numerically computed by a timestepper. It amounts to solving the linearized Navier–Stokes equations for the velocity field $\boldsymbol{u}$ with forcing term $\boldsymbol{f}(t)$ and zero initial conditions.

The observability operator $\mathscr{L}_o : \mathbb{X} \to \mathbb{Y}([0, \infty))$ is defined as

$$\boldsymbol{y}(t) = \mathscr{L}_o(t)\boldsymbol{u}_0 = \mathscr{C}\mathscr{T}(t)\boldsymbol{u}_0. \tag{2.20}$$

This operator describes the mapping of any initial velocity field $\boldsymbol{u}_0$ to the output signal $\boldsymbol{y}(t)$ with $t \geqslant 0$. The output space $\mathbb{Y}([0, \infty))$ contains output trajectories in the future time $t \in [0, \infty)$. The action of $\mathscr{L}_o(t)$ can also be numerically computed and it amounts to extracting the output signal while solving the linearized Navier–Stokes equations with the initial condition $\boldsymbol{u}_0$ at the reference time $t = 0$ and zero forcing.

A direct mapping between input and output can be obtained as the combination of the operators just introduced (see figure 2):

$$\boldsymbol{y}(t) = \mathscr{L}_o\mathscr{L}_c\boldsymbol{f}(t) = \int_{-\infty}^{0} \mathscr{C}\mathscr{T}(t-\tau)\mathscr{B}\boldsymbol{f}(\tau)\,\mathrm{d}\tau. \tag{2.21}$$

https://doi.org/10.1017/S0022112008004394 Published online by Cambridge University Press

This expression can be interpreted as a mapping from past inputs to future outputs. It can be shown that (2.21) is the formal solution for a system which is forced by $\boldsymbol{f}(t)$ in the time interval $t \in (-\infty, 0]$, resulting in the flow field $\boldsymbol{u}_0$ at $t = 0$. The output is extracted for $t \geqslant 0$, corresponding to the signal $\boldsymbol{y}(t)$ produced by the initial condition $\boldsymbol{u}_0$. The expression (2.21) is also the starting point for the input-output analysis, leading to systematically finding reduced-order approximations. The mapping from the inputs to the outputs given by (2.21) in terms of $\mathscr{L}_c$ and $\mathscr{L}_o$ is called Hankel operator $\mathscr{H} : \mathbb{U}((-\infty, 0]) \rightarrow \mathbb{Y}([0, \infty))$, i.e.

$$y(t) = \mathscr{L}_o(t)\mathscr{L}_c \boldsymbol{f}(t) = (\mathscr{H}\boldsymbol{f})(t). \tag{2.22}$$

We have two different representations of the input-output behaviour of the flow system: (i) the state-space representation (2.12) and (ii) the Hankel operator $\mathscr{H}$ defined in (2.22). Note that in the latter case it is assumed that the inputs and outputs are not active at the same time.

2.4. *Adjoint equations and operators*

Before issues related to controllability, observability and model reduction can be considered the adjoint linear operators corresponding to $(\mathscr{T}, \mathscr{L}_c, \mathscr{L}_o)$ must be introduced. The adjoint variables provide information about how variations in the velocity field affect the system output. We show that the adjoint operators can be associated with the adjoint linearized Navier–Stokes equations in state-space form, where the role of the inputs and outputs is reversed. The operators $(\mathscr{T}^*, \mathscr{L}_c^*, \mathscr{L}_o^*, \mathscr{C}^*, \mathscr{B}^*)$ and adjoint Navier–Stokes equations are derived in Appendix A. The inner products associated with the Hilbert spaces $\mathbb{X}$, $\mathbb{U}$, $\mathbb{Y}$, $\mathbb{U}((-\infty, 0])$ and $\mathbb{Y}([0, \infty))$ are also given in § A.1 of Appendix A. The adjoint of the linearized Navier–Stokes equations (2.1) associated with inner product (A 2*a*) is

$$-\dot{\boldsymbol{p}} = (\boldsymbol{U}\cdot\nabla)\boldsymbol{p} - (\nabla \boldsymbol{U})^T \boldsymbol{p} + \nabla\sigma + Re^{-1}\nabla^2 + \lambda(x)\boldsymbol{p}(\boldsymbol{x}), \tag{2.23a}$$

$$0 = \nabla\cdot\boldsymbol{p}, \tag{2.23b}$$

$$\boldsymbol{p} = \boldsymbol{p}_T \qquad \text{at} \quad t = T, \tag{2.23c}$$

This system of equations describes the evolution of adjoint flow field $\boldsymbol{p}(\boldsymbol{x}, t) = (u^*, v^*)^T$ backwards in time. The term σ denotes the adjoint pressure field. The boundary conditions for $\boldsymbol{p}$ are given in § A.1 of Appendix A.

The evolution operator associated with (2.23) is

$$\boldsymbol{p}(\boldsymbol{x}, s - t) = \mathscr{T}^*(t)\boldsymbol{p}(\boldsymbol{x}, s), \tag{2.24}$$

so that given an adjoint field at time s the adjoint evolution operator provides a solution at an earlier time $s - t$. Again, the above operator is approximated numerically using a timestepper solving (2.23). In § A.1 of Appendix A it is shown that $\mathscr{T}^*$ is in fact the adjoint of $\mathscr{T}$ under the inner product (A 2*a*). Furthermore, the infinitesimal generator $\mathscr{A}^*$ of $\mathscr{T}^*$ is the adjoint of $\mathscr{A}$ given in (2.5) (Pazy 1983).

The adjoint linearized Navier–Stokes equations and their corresponding evolution operator form the basis of the adjoint input-output system dual to (2.12). This can be obtained in three steps: (i) derive the adjoint input and output operators $\mathscr{B}^*$ and $\mathscr{C}^*$; (ii) use $\mathscr{B}^*$, $\mathscr{C}^*$ and $\mathscr{T}^*$ to derive the adjoint controllability and observability operator $\mathscr{L}_c^*$ and $\mathscr{L}_o^*$; and (iii) identify the adjoint state space with the system which is associated with $\mathscr{L}_c^*$ and $\mathscr{L}_o^*$.

https://doi.org/10.1017/S0022112008004394 Published online by Cambridge University Press

The adjoint of the input and output operators $\mathscr{B}$ and $\mathscr{C}$ associated with the inner products (A 2*b*) and (A 2*c*) are

$$\mathscr{C}^* = (\mathscr{C}_1^*, \mathscr{C}_2^*) = (h(\boldsymbol{x};\boldsymbol{x}_z), h(\boldsymbol{x};\boldsymbol{x}_v)) \tag{2.25}$$

and

$$\mathscr{B}^*\boldsymbol{p} = \begin{pmatrix} \mathscr{B}_1^*\boldsymbol{p} \\ 0 \\ \mathscr{B}_2^*\boldsymbol{p} \end{pmatrix} = \int_\Omega \begin{pmatrix} h(\boldsymbol{x};\boldsymbol{x}_w)^T\boldsymbol{p} \\ 0 \\ h(\boldsymbol{x};\boldsymbol{x}_u)^T\boldsymbol{p} \end{pmatrix} \mathrm{d}x\,\mathrm{d}y, \tag{2.26}$$

respectively.

The adjoint controllability and observability operators $\mathscr{L}_c^* : \mathbb{X} \to \mathbb{U}((-\infty, 0])$ and $\mathscr{L}_o^* : \mathbb{Y}([0,\infty)) \to \mathbb{X}$ associated with the inner products (A 2*b*) and (A 2*c*) (derived in § A.2 of Appendix A) are given by

$$\mathscr{L}_c^*(-t)\boldsymbol{p}(\boldsymbol{x},0) = \mathscr{B}^*\mathscr{T}^*(-t)\boldsymbol{p}(\boldsymbol{x},0), \tag{2.27a}$$

$$\mathscr{L}_o^*\boldsymbol{t}(t) = \int_0^\infty \mathscr{T}^*(\tau)\mathscr{C}^*\boldsymbol{t}(\tau)\,d\tau, \tag{2.27b}$$

where $\boldsymbol{t} \in \mathbb{Y}$ and $\boldsymbol{p} \in \mathbb{X}$. The first mapping, $\mathscr{L}_c^*$, is from the adjoint state at time $t=0$ onto a signal in $\mathbb{U}$ at time $-t$. The mapping $\mathscr{L}_o^*$ is from an output signal in $\mathbb{Y}$ in $t \in [0,\infty)$ to a state in $\mathbb{X}$ at $t=0$. In analogy to the case of the forward problem defined by (2.12), it can be seen that these two mappings are the observability and controllability operators of the following state-space system:

$$-\dot{\boldsymbol{p}} = \mathscr{A}^*\boldsymbol{p} + \mathscr{C}^*\boldsymbol{t}, \tag{2.28a}$$

$$\boldsymbol{e} = \mathscr{B}^*\boldsymbol{p}. \tag{2.28b}$$

This system has two inputs contained in the vector $\boldsymbol{t} = (z^*, v^*)$ with $\boldsymbol{t} \in \mathbb{Y}$ and three outputs contained in the vector $\boldsymbol{e} = (w^*, u^*, g^*) \in \mathbb{U}$. Comparing the above adjoint equations with (2.12) we observe that the outputs and inputs have exchanged places. In the dual system (2.28), the adjoint flow field is forced by the outputs; the adjoint problem is then used to identify flow fields yielding the largest output response (Dullerud & Paganini 1999).

3. Input–output analysis

In this section, the main input-output characteristics of our problem are analysed in order to identify the modes to retain in a low-order model. We introduce the concepts of Gramians and balancing, using the operators defined in the previous section. For a more detailed presentation of systems theory please refer to Kailath (1980) and Curtain & Zwart (1995). The analysis amounts to computing the eigenmodes of three operators: $\mathscr{L}_c\mathscr{L}_c^*$, $\mathscr{L}_o^*\mathscr{L}_o$ and $\mathscr{L}_c\mathscr{L}_c^*\mathscr{L}_o^*\mathscr{L}_o$. The three sets of modes correspond to the flow structures that are the most easily influenced by the input (controllable modes), the states that produce the largest output energy (observable modes) and the most relevant states for the input-output behaviour (balanced modes). For the sake of clarity, we will show numerical results obtained using only the first input $\mathscr{B}_1$ and the first output $\mathscr{C}_1$, i.e. single-input and single-output system (SISO). We will return to the multi-input multi-output (MIMO) state-space system with input vector $\boldsymbol{f}$ and output vector $\boldsymbol{y}$ in § 4. The three sets of eigenmodes mentioned above can be computed numerically for systems with many degrees of freedom by using the following two approximations:

https://doi.org/10.1017/S0022112008004394 Published online by Cambridge University Press

(i) 'The timestepper': As mentioned above, solutions of Navier–Stokes system (2.12) in input–output form are obtained numerically, using a forward timestepper, which approximates the action of evolution operator $\mathscr{T}$. An adjoint timestepper is used for computing solutions of the associated adjoint system (2.28) and the action of the adjoint evolution operator $\mathscr{T}^*$. The numerical code employed is described in Appendix C. In the simulations presented, we have used 768 collocation points in the streamwise direction x and 101 points in the wall normal direction y, with a computational box of dimensions $L_x = 1000$ and $L_y = 30$ (see figure 1). The discretized system has thus $m \approx 10^5$ degrees of freedom.

(ii) 'The snapshot method': The controllable and observable modes introduced next are computed using the snapshot method introduced by Sirovich (1987). Recently Rowley (2005) extended this method to obtain balanced modes. The snapshot technique is described in Appendix B. For the results presented, the flow structures are computed by collecting 1600 snapshots of the forward simulation, using each input as initial condition, and 1600 snapshots of the adjoint simulation, using each output as initial condition. The snapshots were taken with equal spacing in the time interval (0, 4000).

3.1. *Controllable modes*

We begin our input–output analysis by searching for flow states that are most easily triggered by a given input. This issue is related to the concept of controllability, which, in general, quantifies the possibility of steering the flow between two arbitrary states. A state $\boldsymbol{u}$ is controllable if it belongs to the range of $\mathscr{L}_c$; that is $\boldsymbol{u} = \mathscr{L}_c \boldsymbol{f}(t)$ exists for some $\boldsymbol{f}(t)$†. A commonly adopted interpretation of controllability is illustrated by the following optimal control problem: what is the minimum input energy $\|\boldsymbol{f}\|^2_{\mathbb{U}((-\infty,0])}$ in the time span $t \in (-\infty, 0]$ required to bring the state (if possible) from zero to the given initial condition $\boldsymbol{u}(\boldsymbol{x}, 0) = \boldsymbol{u}_0$?

Assuming that $\boldsymbol{u}_0(\boldsymbol{x})$ has a unit norm and that it is controllable, it can be shown‡ that the optimal input is given by

$$\boldsymbol{f} = \mathscr{L}_c^* \mathscr{P}^{-1} \boldsymbol{u}_0, \tag{3.1}$$

where $\mathscr{P}$ is the controllability Gramian defined as

$$\mathscr{P} = \mathscr{L}_c \mathscr{L}_c^* = \int_{-\infty}^{0} \mathscr{T}(-t)\mathscr{B}\mathscr{B}^*\mathscr{T}^*(-t)\,\mathrm{d}t = \int_{0}^{\infty} \mathscr{T}(t)\mathscr{B}\mathscr{B}^*\mathscr{T}^*(t)\,\mathrm{d}t. \tag{3.2}$$

In the first equality (2.19) and (2.27*a*) have been used. Using (3.1) the minimum input energy is given by

$$\|\boldsymbol{f}\|^2_{\mathbb{U}((-\infty,0])} = \int_{\Omega} \boldsymbol{u}_0^T \mathscr{P}^{-1} \boldsymbol{u}_0 \,\mathrm{d}x\,\mathrm{d}y. \tag{3.3}$$

The controllability Gramian $\mathscr{P}$ provides a means to rank different states according to how easily they can be influenced by an input. In particular, the most easily influenced, or the most controllable, flow structures are the eigenfunctions of $\mathscr{P}$

† The system (2.12) is called exactly controllable if all states $\boldsymbol{u} \in \mathbb{X}$ can be reached for some input. This is rarely the case for elliptic/parabolic PDEs, and a less restrictive condition is approximate controllability, where any state $\boldsymbol{u} \in \mathbb{X}$ can be approximated arbitrary closely by controllable elements (Curtain & Zwart 1995).

‡ For the finite-dimensional case see Lewis & Syrmos (1995) and Dullerud & Paganini (1999). In the general case $\mathscr{P}^{-1}$ is well defined on any finite-dimensional subspace of $\mathbb{X}$.

https://doi.org/10.1017/S0022112008004394 Published online by Cambridge University Press

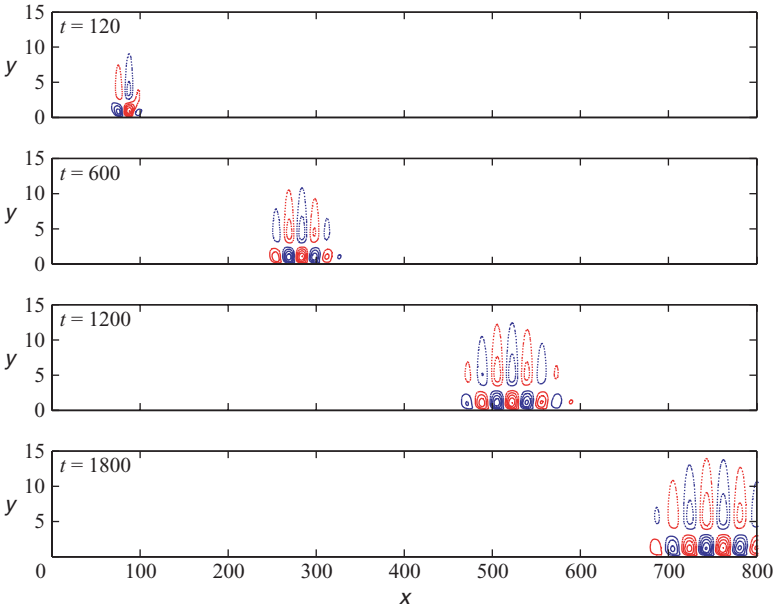


FIGURE 3. Instantaneous snapshots of the streamwise disturbance component at $t = 120$, 600, 1200 and 1800 triggered by an impulse in $\mathscr{B}_1$.

associated with the largest eigenvalues of

$$\mathscr{P}\boldsymbol{\phi}_i^c = \lambda_i^c \boldsymbol{\phi}_i^c. \tag{3.4}$$

The superscript c stands for controllable modes. Note that $\mathscr{P}$ is a self-adjoint and positive semi-definite operator whose eigenvalues are real and positive and the eigenfunctions mutually orthogonal. If $\lambda_i^c \ll 1$, the corresponding eigenfunction $\boldsymbol{\phi}_i^c$ requires very large energy to be excited by the input, since $(\lambda_i^c)^{-1}$ is proportional to $\|\boldsymbol{f}\|_{\mathbb{U}((-\infty,0])}$. The mode is then referred to as (nearly) uncontrollable.

For linear systems the controllability Gramian corresponds to the covariance of the state response to an impulse in time. Therefore, the controllable modes can be regarded as POD modes (Ilak & Rowley 2008; Bagheri *et al.* 2008). Traditionally, the interpretation of these modes is that they represent decorrelated energy-ranked flow states. For example the first POD mode $\boldsymbol{\phi}_1^c$ is the most energetic structure in the flow, containing $\lambda_1^c / \sum_{i=1}^{\infty} \lambda_i^c \times 100\,\%$ of the total flow energy. These modes can be conveniently obtained by collecting r snapshots of the flow at discrete times $t_1, \ldots, t_r$ and solving an $r \times r$ eigenvalue problem (Sirovich 1987).

The controllable modes can thus be computed from the response of the flow to an impulse, $\delta(0)$:

$$\boldsymbol{u}(\boldsymbol{x}, t_j) = \mathscr{T}(t_j)\mathscr{B}_1. \tag{3.5}$$

The impulse response can be used to build the Gramian and compute the most controllable modes as shown in Appendix B. Figure 3 shows the streamwise velocity component of the instantaneous velocity field after an impulse from $\mathscr{B}_1$ at four different times. The generation and convection of a wavepacket with a dominant spatial wavenumber and a propagation speed of about $0.4U_\infty$ can be observed. The wavepacket grows in amplitude and size in the x direction, until it reaches the beginning of the fringe region at $x = 800$. As it enters this region, the disturbance is

https://doi.org/10.1017/S0022112008004394 Published online by Cambridge University Press

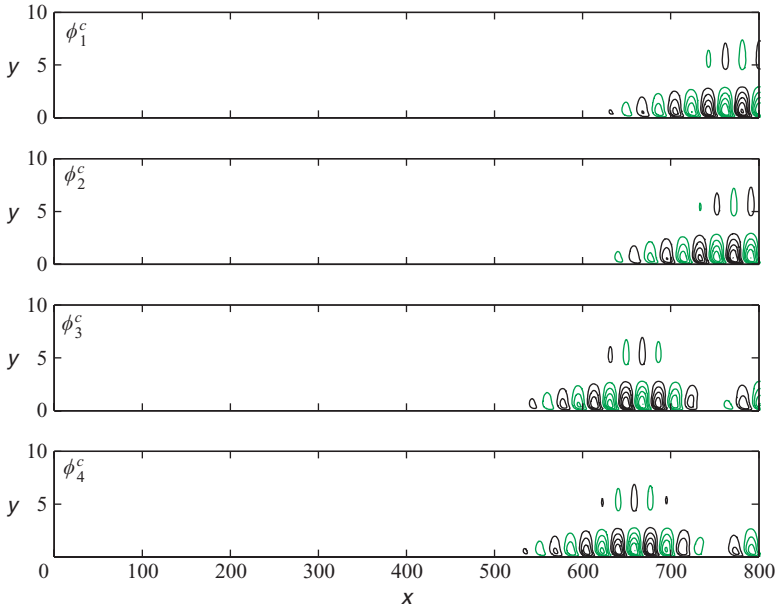


FIGURE 4. The streamwise component of the four most controllable modes $\boldsymbol{\phi}_i^c$.

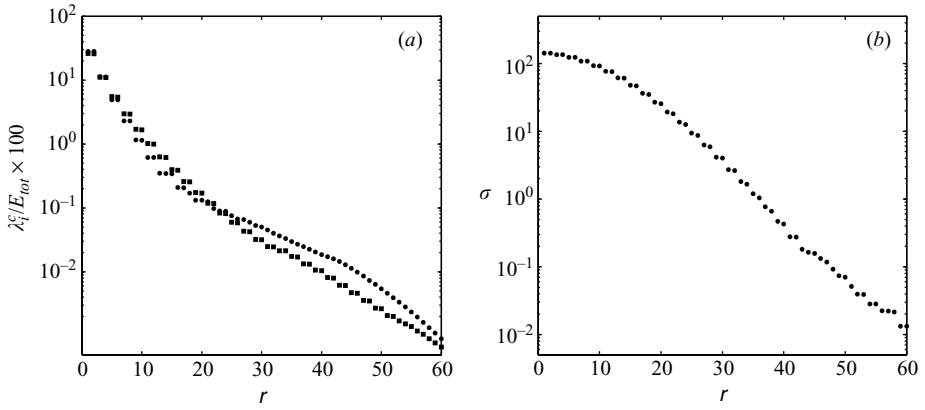


FIGURE 5. (*a*) The normalized eigenvalues λ_i^c (squares) and λ_i^o (circles) associated with controllable modes and observable modes respectively. (*b*) The Hankel singular values σ_i corresponding to the balanced modes.

eventually damped by the fringe forcing, reproducing the effect of an outflow. The input–output system (2.12) is thus asymptotically stable.

The u component of the four most controllable modes $\boldsymbol{\phi}_i^c$ with respect to $\mathscr{B}_1$ are shown in figure 4, while the corresponding eigenvalues λ_i^c are displayed in figure 5(*a*) with square symbols. The first 20 controllable modes contain 99 % of the flow energy, meaning that a significant part of the controllable subspace is spanned by 20 modes. Note that the flow structures that are the most easily influenced by the input $\mathscr{B}_1$ are located downstream in the domain, where the energy of the response to forcing is the largest. In other words, low energy is needed at location $\mathscr{B}_1$ to force

https://doi.org/10.1017/S0022112008004394 Published online by Cambridge University Press

large structures downstream owing to the amplification provided by the intrinsic flow dynamics. Moreover, the eigenvalues shown in figure 5 come in pairs. The corresponding velocity fields (see the first and the second modes in figure 4) have the same wavepacket structure 90° out of phase. These modes represent travelling structures (see also Rempfer & Fasel 1994).

3.2. *Observable modes*

For a given sensor it is important to determine whether the relevant flow instabilities can be detected, and if so, to which accuracy. The flow fields which can be most easily detected are called the most observable modes†. As in the case of the controllability Gramian, the observability problem can also be cast as an optimization problem. We wish to find the initial conditions that produce the largest output energy. The output energy generated by the initial condition $\boldsymbol{u}_0$, assumed to be of unit norm, is given by

$$\|\boldsymbol{y}\|^2_{\mathbf{Y}([0,\infty))} = \langle \mathscr{L}_o \boldsymbol{u}_0, \mathscr{L}_o \boldsymbol{u}_0 \rangle_{\mathbf{Y}([0,\infty))} = \langle \boldsymbol{u}_0, \mathscr{L}_o^* \mathscr{L}_o \boldsymbol{u}_0 \rangle_{\mathbf{X}} = \int_\Omega \boldsymbol{u}_0^T \underbrace{\mathscr{L}_o^* \mathscr{L}_o}_{\mathscr{Q}} \boldsymbol{u}_0 \, \mathrm{d}x \, \mathrm{d}y, \quad (3.6)$$

where $\mathscr{Q}$ is called the observability Gramian. Using (2.20) and (2.27*b*) we obtain the following expression for $\mathscr{Q}$:

$$\mathscr{Q} = \mathscr{L}_o^* \mathscr{L}_o = \int_0^\infty \mathscr{T}^*(t) \mathscr{C}^* \mathscr{C} \mathscr{T}(t) \, \mathrm{d}t. \quad (3.7)$$

The observability Gramian provides a means to rank states according to their contribution to the output. The most observable state $\boldsymbol{\phi}_1^o$ is given by the eigenfunction of the operator $\mathscr{Q}$ corresponding to the largest eigenvalue of

$$\mathscr{Q} \boldsymbol{\phi}_i^o = \lambda_i^o \boldsymbol{\phi}_i^o. \quad (3.8)$$

The superscript o stands for observable modes. Note that $\mathscr{Q}$ is a self-adjoint and positive semi-definite operator so that its eigenvalues are real and positive and its eigenfunctions mutually orthogonal. The most observable mode $\boldsymbol{\phi}_1^o$ contributes $\lambda_1^o / \sum_{j=0}^\infty \lambda_j^o \times 100\,\%$ to the total sensor energy; the second most observable mode $\boldsymbol{\phi}_2^o$ contributes $\lambda_2^o / \sum_{j=0}^\infty \lambda_j^o \times 100\,\%$; and so on. In particular, if $\lambda_i^o \ll 1$, the corresponding mode $\boldsymbol{\phi}_i^o$ does not make a contribution to sensor output and is called a (nearly) unobservable mode. Note that the observable modes can be regarded as POD modes of the adjoint system.

From the definition of $\mathscr{Q}$ in (3.7) it follows that the observable modes pertaining to a given output can be determined from the impulse response of one adjoint simulation (see Appendix B). The results of this simulation, $\mathscr{T}^*(t)\mathscr{C}^*$, can then be used to build the second-order correlation of the flow field, $\mathscr{T}^*(t)\mathscr{C}^*\mathscr{C}\mathscr{T}(t)$, and thus the Gramian. The eigenvalue problem (3.8) is solved by using the snapshot method as explained earlier for the case of the controllable modes. Here we present results for the first output $\mathscr{C}_1$ only. Figure 6 shows the instantaneous adjoint field at four different times

$$\boldsymbol{p}(\boldsymbol{x}, -t_j) = \mathscr{T}^*(t_j) \mathscr{C}_1^*, \quad (3.9)$$

after an impulse from the first output, i.e. $\mathscr{C}_1^* \delta(0)$. The triggered wavepacket travels backward in time in the upstream direction with upstream-tilted structures. The adjoint solution can be regarded as the sensitivity of the output $\mathscr{C}_1$ with respect to linear perturbations to the underlying base flow. In other words, the flow structures

† The system (2.12) is approximately observable if $\mathscr{L}_o \boldsymbol{u} = 0$ occurs only when $\boldsymbol{u} = 0$, i.e. if the knowledge of the output determines the initial state uniquely (Curtain & Zwart 1995).

https://doi.org/10.1017/S0022112008004394 Published online by Cambridge University Press

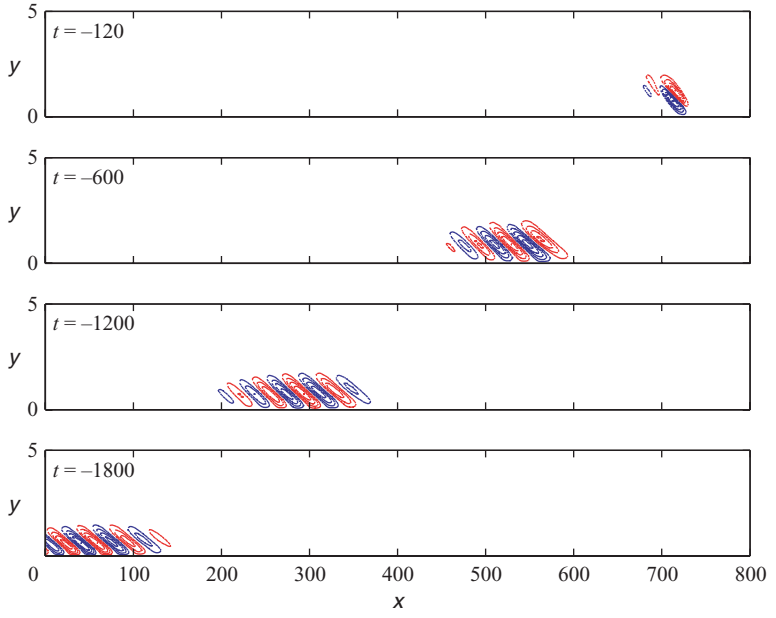


FIGURE 6. Instantaneous snapshots of the streamwise disturbance component at $t = -120, -600, -1200$ and -1800 of the adjoint impulse in $\mathscr{C}_1$.

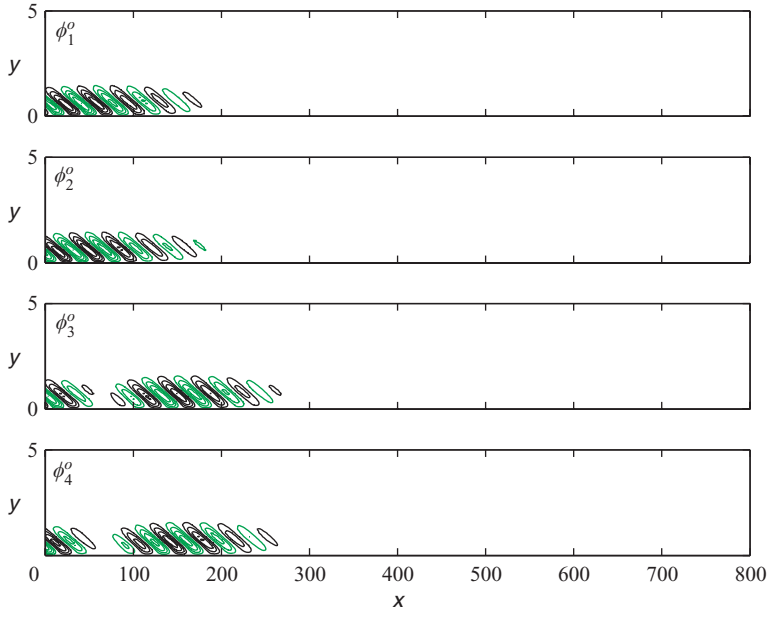


FIGURE 7. The streamwise velocity component of the four most observable modes $\boldsymbol{\phi}_i^o$.

excited by $\mathscr{C}_1^*$ and shown in figure 6 are also the structures to which the sensor $\mathscr{C}_1$ is the most sensitive. In this context, the negative time can be interpreted as the delay between the time these structures are present and the instant they can be measured.

The u component of the four most observable modes $\boldsymbol{\phi}_i^o$ with respect to $\mathscr{C}_1$ is shown in figure 7, while the associated eigenvalues are reported as circles in figure 5(a). From the latter figure, we observe that the leading 20 modes are responsible for nearly

https://doi.org/10.1017/S0022112008004394 Published online by Cambridge University Press

the entire output energy. The flow structures in figure 7 are initial conditions that contribute with the most energy to the sensor output. These modes are real-valued functions, and therefore two of them are needed to describe travelling flow structures, which explains the appearance of pairs of eigenvalues in figure 5(*a*). There are two further noteworthy remarks:

(i) The spatial support of the observable modes is far upstream, where the sensitivity of the flow is the largest. Hence, the most observable structures are spatially disconnected from the most controllable modes. This spatial separation is also observed between the global eigenmodes of the linearized Navier–Stokes equations and eigenmodes of the adjoint Navier–Stokes, where it is associated with streamwise non-normality of the system (Chomaz 2005).

(ii) The most observable structures are tilted in the upstream direction, 'leaning' against the shear layer, and are similar to the linear optimal disturbances computed by Åkervik *et al.* (2008). The optimal disturbance is the initial condition maximizing the perturbation energy over the entire domain Ω at a fixed time $t = T$. On the other hand, observable modes maximize the time integral of the perturbation energy in the region defined by the output $\mathscr{C}_1$. Choosing the sensor location in correspondence to the largest flow response leads therefore to the similarity between linear optimals and observable modes. As noticed by Butler & Farrell (1992), the upstream tilting of the optimal initial conditions can be attributed to the wall normal non-normality of the governing operator; perturbations extract energy from the mean shear by transporting momentum down the mean velocity gradient (the so-called Orr mechanism).

3.3. *Balanced modes*

So far we have identified modes that characterize either the response to forcing or the sensitivity of an output. In this section we present the balanced modes (Moore 1981), which take into account both the response behaviour and the output sensitivity. Similar to the previous section, we wish to excite the largest output energy. However, rather than identifying dangerous initial conditions, using the mapping $\mathscr{L}_o$ as in (3.6), we look directly for input signals which produce the largest output energy via the input-output mapping $\mathscr{L}_o\mathscr{L}_c$ given in (2.22).

The output energy generated by the past input $\boldsymbol{f}$, assumed to be of unit norm, is given at time t by

$$\|\boldsymbol{y}\|^2_{\mathbb{Y}([0,\infty))} = \langle \mathscr{H}\boldsymbol{f}, \mathscr{H}\boldsymbol{f}\rangle_{\mathbb{Y}([0,\infty))} = \langle \boldsymbol{f}, \mathscr{H}^*\mathscr{H}\boldsymbol{f}\rangle_{\mathbb{U}((-\infty,0])} = \int_{-\infty}^{0} \boldsymbol{f}^T \mathscr{H}^*\mathscr{H}\boldsymbol{f}\,\mathrm{d}t. \tag{3.10}$$

If we let the sequence of input vectors $\boldsymbol{f}_i$ with unit norm represent the eigenfunctions of $\mathscr{H}^*\mathscr{H}$, i.e.

$$\mathscr{H}^*\mathscr{H}\boldsymbol{f}_i = \sigma_i^2\boldsymbol{f}_i, \tag{3.11}$$

then the output energy will be given by the square of the so-called Hankel singular values (HSV) σ_i. The most dangerous input vector $\boldsymbol{f}_1$ with $\|\boldsymbol{f}_1\|_{\mathbb{U}((-\infty,0])} = 1$ thus results in an output signal which has been amplified by σ_1^2. Note that $\sigma_1 \geqslant \sigma_2 \geqslant \ldots$, so the eigenmodes of the input-output map are ranked according to how much the input signal is amplified, as it is filtered by the linear system and the output.

Using the controllability operator $\mathscr{L}_c$ we obtain the flow structure associated with the forcing $\boldsymbol{f}_i$:

$$\boldsymbol{\phi}_i^{oc} = \frac{1}{\sqrt{\sigma_i}}\mathscr{L}_c\boldsymbol{f}_i. \tag{3.12}$$

https://doi.org/10.1017/S0022112008004394 Published online by Cambridge University Press

Notice that $\sigma^{-1/2}$ is a convenient normalization factor. The modes are denoted by the superscript *oc*, which indicates that these modes are both observable and controllable. The sequence of functions $\boldsymbol{\phi}_i^{oc}$ are called the balanced modes, and as we show next, they diagonalize the observability Gramian. Computing the output energy for $\mathbf{f}_i$ and using (3.12), we obtain

$$\int_{-\infty}^{0} \mathbf{f}_i^T \mathscr{H}^* \mathscr{H} \mathbf{f}_i \,\mathrm{d}t = \sqrt{\sigma_i} \langle \mathbf{f}_i, \mathscr{L}_c^* \mathscr{Q} \boldsymbol{\phi}_i^{oc} \rangle_{\mathbb{U}((-\infty,0])} = \sigma_i \langle \boldsymbol{\phi}_i^{oc}, \mathscr{Q} \boldsymbol{\phi}_i^{oc} \rangle_{\mathbb{X}} = \sigma_i^2, \tag{3.13}$$

where the definitions $\mathscr{H} = \mathscr{L}_o \mathscr{L}_c$, $\mathscr{H}^* = \mathscr{L}_c^* \mathscr{L}_o^*$ and $\mathscr{Q} = \mathscr{L}_o^* \mathscr{L}_o$ are used. A diagonal observability Gramian implies that these modes can be regarded as orthogonal if this Gramian is used as inner-product weight matrix. With respect to inner product defined in (A 2*a*), however, these modes are not orthogonal.

A sequence of functions $\boldsymbol{\psi}_i^{oc}$, referred to as the adjoint balanced modes, which is bi-orthogonal to $\boldsymbol{\phi}_i^{oc}$ according to

$$\left\langle \boldsymbol{\psi}_i^{oc}, \boldsymbol{\phi}_j^{oc} \right\rangle_{\mathbb{X}} = \delta_{i,j}, \tag{3.14}$$

is needed to project our system on the basis given by the balanced modes. The derivation is analogous to $\boldsymbol{\phi}_i^{oc}$, but now we consider instead the left eigenvectors $\mathbf{s}_i$ of the input-output map $\mathscr{H}^* \mathscr{H}$, i.e.

$$\mathscr{H} \mathscr{H}^* \mathbf{s}_i = \mathbf{s}_i \sigma_i^2. \tag{3.15}$$

The adjoint balanced modes are then given by

$$\boldsymbol{\psi}_i^{oc} = \frac{1}{\sqrt{\sigma_i}} \mathscr{L}_o^* \mathbf{s}_i. \tag{3.16}$$

It is possible to show by the same procedure used in (3.13) that these modes diagonalize the controllability Gramian:

$$\langle \boldsymbol{\psi}_i^{oc}, \mathscr{P} \boldsymbol{\psi}_i^{oc} \rangle_{\mathbb{X}} = \sigma_i. \tag{3.17}$$

Furthermore, the diagonal elements are also equal to the Hankel singular values. The term balancing now becomes clear; using $\boldsymbol{\phi}_i^{oc}$ and $\boldsymbol{\psi}_i^{oc}$ the controllability and observability Gramians become diagonal and equal to the HSV. In other words, the observability and controllability properties are balanced. This is useful for performing model reduction, as it allows us to discard the modes which are both difficult to measure and difficult to excite by the inputs.

To compute these modes, it is convenient to show that $\boldsymbol{\phi}_i^{oc}$ are the eigenmodes of $\mathscr{P}\mathscr{Q}$; multiplying (3.11) with $\mathscr{L}_c$ yields

$$\mathscr{L}_c \mathscr{H}^* \mathscr{H} \mathbf{f}_i = \mathscr{P} \mathscr{Q} \boldsymbol{\phi}_i^{oc} = \sigma_i^2 \boldsymbol{\phi}_i^{oc}. \tag{3.18}$$

The computation of the balanced modes and their associated adjoints can again be accomplished using a timestepper and the snapshot method described in Appendix B. In this case one combines the sequence of snapshots collected from the solution of the forward problem (2.12) with a sequence of snapshots collected from the adjoint system (2.28). In this way we can approximate the eigenvalue problem (3.18) to obtain the balanced modes (Rowley 2005). The u component of the first four balanced modes $\boldsymbol{\phi}_i^{oc}$ with respect to $\mathscr{B}_1$ and $\mathscr{C}_1$ are shown in figure 8 and the corresponding adjoint modes $\boldsymbol{\psi}_i^{oc}$ in figure 9. The HSV σ_i are shown in figure 5(*b*). As in the case of the observability and controllability eigenvalues λ_i^c and λ_i^o, the singular values come in pairs, indicating that the leading balanced modes are travelling structures. The same observation was made by Ilak & Rowley (2008) for channel flow.

https://doi.org/10.1017/S0022112008004394 Published online by Cambridge University Press

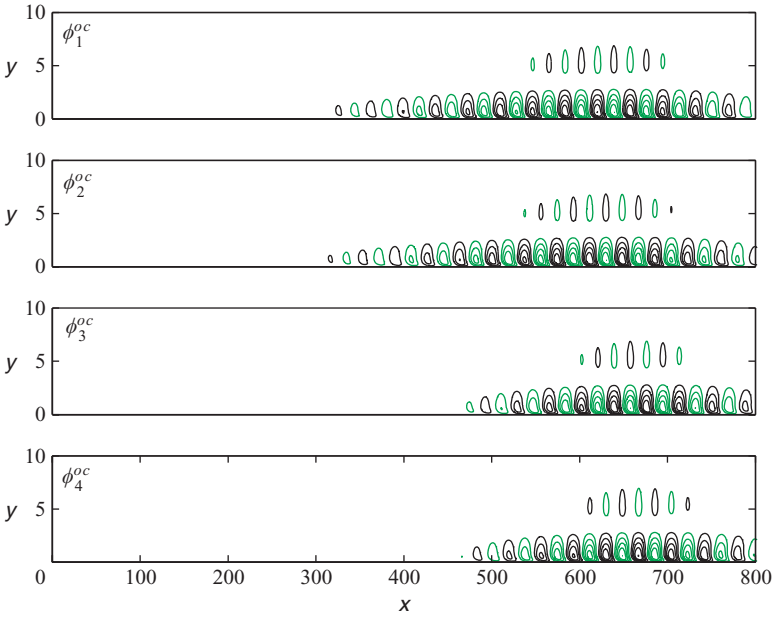


FIGURE 8. The streamwise velocity component of the first four balanced modes $\boldsymbol{\phi}_i^{oc}$.

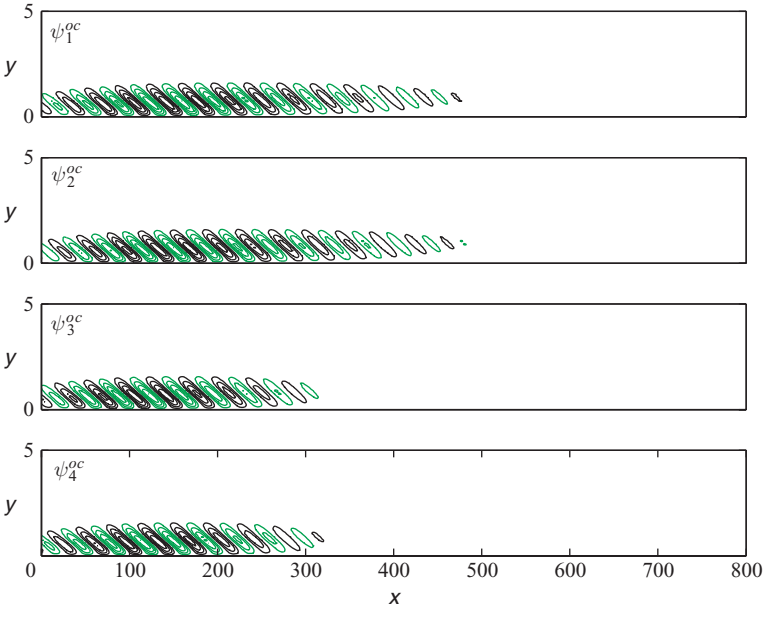


FIGURE 9. The streamwise velocity component of the adjoint balanced modes $\boldsymbol{\psi}_i^{oc}$.

From figures 8 and 9 we observe that the leading balanced modes appear also as wavepackets, but they are somewhat more spatially extended than the controllable POD modes (figure 4). Similarly, the adjoint balanced modes have a larger spatial support than the observable modes (figure 7). As noticed by Ahuja *et al.* (2007) and Ilak & Rowley (2008), we can account for both controllability and observability through the non-orthogonality of the balanced modes. In the two previous sections we

https://doi.org/10.1017/S0022112008004394 Published online by Cambridge University Press

observed that for an input $\mathscr{B}_1$ located upstream and an output $\mathscr{C}_1$ located downstream, the associated controllable and observable modes are spatially located in different parts of the domain. The controllable subspace and the observable subspace are thus separated in the streamwise direction. This is a consequence of the convective nature of the instabilities arising in the Blasius flow in which disturbances grow in amplitude, as they are convected in the downstream direction. Essentially, this separation implies that the distribution of both the input and the output cannot be captured by an orthogonal projection onto the leading modes of only one subspace. Conversely, in a bi-orthogonal projection the adjoint balanced modes account for the output sensitivity and the direct balanced modes for the most energetic structures.

4. Model reduction

Since the disturbances are represented by an input, and the objective consists of minimizing an output signal, capturing the input–output behaviour of the system – described by the mapping $\mathscr{L}_o\mathscr{L}_c$ – is sufficient for the design of optimal and robust control schemes. The flow structures that are neither controllable nor observable are redundant for the input-output behaviour. Moreover, the states that are nearly uncontrollable and nearly unobservable can be discarded, since they have a very weak influence on the input-output behaviour. A systematic approach of approximating the system given by (2.1) with a finite-dimensional model, which preserves the main input-output behaviour, is called balanced truncation (Moore 1981). As we show next, balanced truncation amounts to a projection of state-space system (2.12) on the leading balanced modes.

We now return to the MIMO state-space system with input vector $\boldsymbol{f}$ and output vector $\boldsymbol{y}$. The measurement noise acts on the output signal and affects the perturbation dynamics only in the closed-loop system and is hence not included in the analysis.

4.1. *Galerkin projection*

Any flow field can be approximated as a linear combination of the leading r balanced modes:

$$\boldsymbol{u}^r(\boldsymbol{x},t)=\sum_{j=1}^{r} q_j(t)\boldsymbol{\phi}_j^{oc}(\boldsymbol{x}), \tag{4.1}$$

where $q_j=\langle \boldsymbol{u},\boldsymbol{\psi}_j^{oc}\rangle_{\mathbb{X}}$ is the expansion coefficient. Inserting the above expansion into (2.12) and taking the inner product with the adjoint balanced modes $\boldsymbol{\psi}_i^{oc}$, the following r-dimensional state-space form is obtained:

$$\dot{q}=Aq+B_1w+B_2u, \tag{4.2a}$$
$$v=C_1q+lu, \tag{4.2b}$$
$$z=C_2q+\alpha g\,. \tag{4.2c}$$

This system is referred to as the ROM. The column vector q contains q_j, and the entries of the matrix A, column vector B_1 and row vector C_1 are

$$A_{i,j}=\left\langle \boldsymbol{\psi}_i^{oc},\mathscr{A}\boldsymbol{\phi}_j^{oc}\right\rangle_{\mathbb{X}}, \tag{4.3a}$$
$$B_{1,j}=\left\langle \boldsymbol{\psi}_j^{oc},\mathscr{B}_1\right\rangle_{\mathbb{X}}, \tag{4.3b}$$
$$C_{1,j}=\mathscr{C}_1\boldsymbol{\phi}_j^{oc} \tag{4.3c}$$

https://doi.org/10.1017/S0022112008004394 Published online by Cambridge University Press

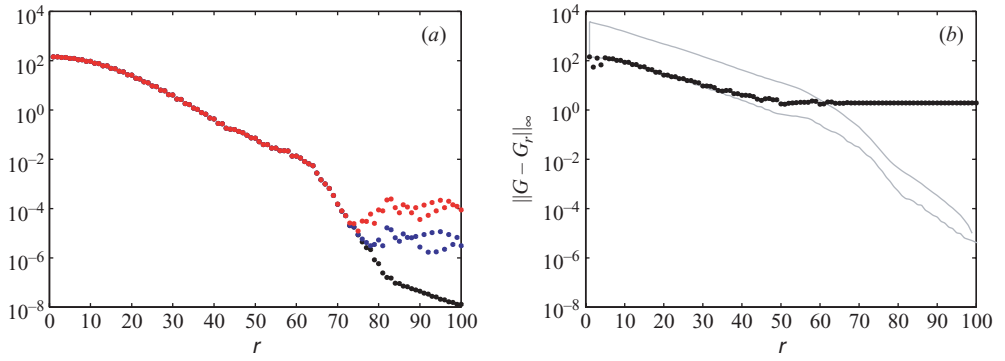


FIGURE 10. (*a*) The Hankel singular values (black symbols) are compared to the diagonal entries of the controllability (red) and observability (blue) Gramians associated with the balanced reduced-order system. (*b*) The $\mathscr{H}_\infty$ model reduction error. The upper and lower theoretical bounds are depicted with grey lines, and the actual model reduction error is shown with black symbols.

for $i, j = 1, \ldots, r$. The components of the vectors C_2 and B_2 are obtained in the same manner as those of B_1 and C_1. The evolution operator associated with (4.2) is

$$T(t) = \mathrm{e}^{At} = \sum_{j=0}^{\infty} \frac{(At)^j}{j!}. \tag{4.4}$$

Notice that the balanced modes are computed accounting for all the inputs (except the measurement noise) and outputs, and the Galerkin projection (4.2) is performed only once. The projection of $\mathscr{A}$ on the balanced modes can be approximated by the finite-difference method, using the timestepper and (2.5). For the results presented, δt was chosen to be 10^{-4} after a convergence study.

To validate the properties of the snapshot-based balanced truncation, we constructed the reduced model (4.2) and computed its controllability and observability Gramians. The projected system is internally balanced only if its Gramians are diagonal and equal to the HSV. We found that the first 70×70 elements of both Gramians were diagonal. In figure 10 we compare the leading 100 diagonal elements with the HSV. The first 70 modes are observed to be bi-orthogonal to each other down to numerical accuracy. However, for higher modes, as the numerical round-off errors increase, the bi-orthogonality is gradually lost, and off-diagonal elements are observed in both Gramians. By increasing the numerical resolution and the number of snapshots it is possible to increase the number of balanced modes. However, – as noticed by (Moore 1981) – the ratio σ_1/σ_i serves as a condition number for $\boldsymbol{\phi}_i^{oc}$, and therefore the balanced modes corresponding to very small HSV can be ill conditioned independent of the numerical approximations.

4.1.1. *Performance of the ROM*

In this section the input-output behaviour of the ROM (4.2) is compared to the full Navier–Stokes system (2.12). We begin by comparing the impulse response from all inputs to all outputs. In figure 11 three signals $\mathscr{B}_1 \to \mathscr{C}_1$, $\mathscr{B}_1 \to \mathscr{C}_2$ and $\mathscr{B}_2 \to \mathscr{C}_1$ are shown with black lines. The response of $\mathscr{C}_2$ to forcing in $\mathscr{B}_2$ is zero, since disturbances travelling upstream are quickly damped. These impulse responses were obtained by using the timestepper with $\sim 10^5$ degrees of freedom. The impulse responses of the ROM (4.2) with $r = 50$ given by $\boldsymbol{y}(t) = Ce^{At}B$ are shown with red dashed lines. We

https://doi.org/10.1017/S0022112008004394 Published online by Cambridge University Press

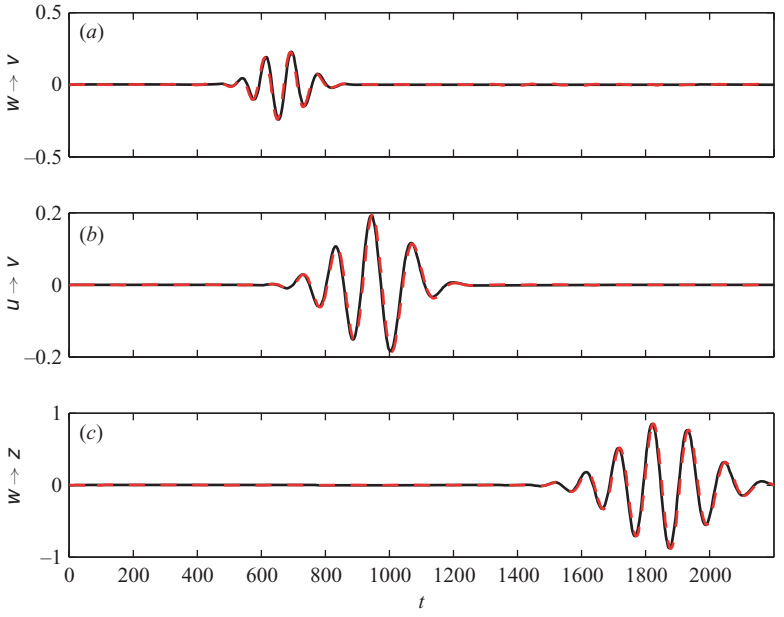


FIGURE 11. The impulse response from $\mathscr{B}_1 \rightarrow \mathscr{C}_2$ (*a*), $\mathscr{B}_2 \rightarrow \mathscr{C}_1$ (*b*) and $\mathscr{B}_1 \rightarrow \mathscr{C}_1$ (*c*). The black solid line represents direct numerical simulations with 10^5 degrees of freedom and the red dashed line the balanced reduced-model with 50 degrees of freedom.

observe that reduced model registers the same signal as the full model from all inputs to all outputs. The wavepacket triggered by the impulse of $\mathscr{B}_1$ reaches the first sensor $\mathscr{C}_2$ after 600 time units and the second sensor $\mathscr{C}_1$ after 1500 time units. The wavepacket triggered from the actuator reaches the second sensor after 600 time units.

The frequency response of the full system and the ROM are compared next. The frequency response is related to the Laplace transform of the impulse response ($\mathscr{B} \rightarrow \mathscr{C}$) (see, e.g. Skogestad & Postlethwaite 2005), which in our case results in the 2×3 transfer function matrix (TFM):

$$G(s) = \mathscr{C}(s - \mathscr{A})^{-1}\mathscr{B} \tag{4.5}$$

with $s \in \mathbb{C}$. The element $G_{i,j}$ contains the response from $\mathscr{B}_j \rightarrow \mathscr{C}_i$. The TFM of size 2×3 of the reduced model is similarly defined as

$$G_r(s) = C(sI - A)^{-1}B \tag{4.6}$$

with I as identity matrix of size r.

Due to the linear nature of the equations, a sinusoidal input signal $\mathrm{e}^{\mathrm{i}\omega t}$ with constant frequency ω will generate an output with the same frequency but with a phase shift $\mathrm{Arg}\{G(\mathrm{i}\omega)\}$ and a different amplitude $|G(\mathrm{i}\omega)|$. The frequency response gain is usually measured by the largest singular value of the TFM (Skogestad & Postlethwaite 2005). For the full model we do not have an explicit expression of the TFM. Therefore, we make use of our timestepper and apply a sinusoidal signal with a constant frequency ω in each input and extract the periodic signal from the outputs once the initial transients have died out. Note that computing the frequency response with the timestepper in this way does not take into account the interaction of input signals, since only one input is active at a time.

https://doi.org/10.1017/S0022112008004394 Published online by Cambridge University Press

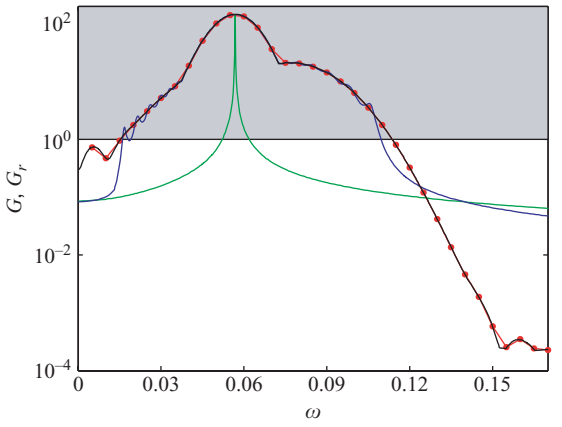


FIGURE 12. The envelope of the MIMO transfer function matrix $G(\mathrm{i}\omega)$ from all inputs to all outputs computed using the timestepper is shown with red symbols. The largest response is for $\omega = 0.06$ with a peak value of 144.6. For $\omega \in [0, 0.03]$ the frequency response from the actuator to objective function ($\mathscr{B}_2 \to \mathscr{C}_1$) dominates. The frequencies with the largest gain are obtained from disturbances to objective function ($\mathscr{B}_1 \to \mathscr{C}_1$) in the range $\omega \in [0.03, 0.07]$, and finally for higher frequencies the response from disturbances to measurement sensor ($\mathscr{B}_1 \to \mathscr{C}_2$) are amplified the most. The frequencies in the grey domain are amplified. Also shown are the frequency response (the envelope) of the reduced model TFM $G_r(\mathrm{i}\omega)$ with ranks 2 (green), 50 (blue) and 100 (black).

In figure 12 the envelope of the TFM amplitudes – the largest amplification of all the frequency responses from $\mathscr{B}_1 \to \mathscr{C}_1$, $\mathscr{B}_1 \to \mathscr{C}_2$ and $\mathscr{B}_2 \to \mathscr{C}_1$ at each ω – for the full model of order 10^5 is shown with red filled circles. In the same figure the TFM amplitudes of ROMs of order $r = 2$, 50 and 100 are shown. We observe that the ROM of order 2 captures the most important aspect of the input-output behaviour, which is the response of the most dangerous frequency, i.e. the peak response of the full model. The model with 50 modes is able to estimate the gains of all the amplified frequencies but fails to capture the damped low and high frequencies. Adding 50 additional modes results in a model that preserves the input-output behaviour correctly for all frequencies. Note that there are no isolated eigenvalues in the spectrum of the spatially developing Blasius flow (Ehrenstein & Gallaire 2005; Åkervik *et al.* 2008), and therefore the frequency response is rather smooth with no peaks. Low-pass filters of this form cannot be represented with only a few degrees of freedom.

Finally, the model reduction error is computed and compared to the theoretical bounds given by the Hankel singular values. An attractive feature of balanced truncation is the existence of error bounds (which are obtained *a priori* to Galerkin projection):

$$\sigma_{r+1} < \|G - G_r\|_\infty \leqslant 2 \sum_{j=r+1}^{n} \sigma_j. \tag{4.7}$$

The infinity norm of the transfer function equals the peak value of the frequency response gain based on the largest singular value, i.e.

$$\|G(s)\|_\infty = \max_\omega \sigma_1(G(i\omega)). \tag{4.8}$$

Estimating the model reduction error (4.7) amounts to the calculation of the difference of the peak values of frequency response of the reduced-order and the Navier–Stokes

https://doi.org/10.1017/S0022112008004394 Published online by Cambridge University Press

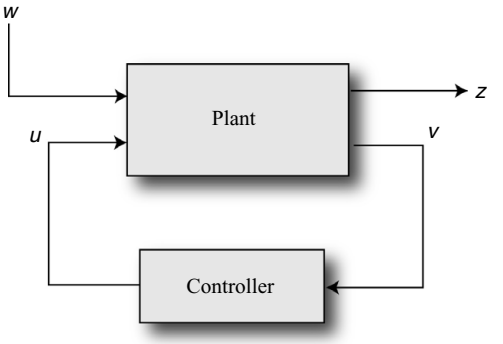


FIGURE 13. The closed-loop system. The plant represents the input-output system given by (2.12) subject to external disturbances w. The controller of the order 50 forces the Navier–Stokes equations with the input signal u based on the noisy measurements v, so that the effect of w on the output signal z is minimized.

systems. For the latter system, we use the peak value of the amplitude envelope as shown in figure 12 instead of the largest singular value. The error norm for the balanced truncation model is shown in figure 10(b) with black symbols. The error norm is close to the lower bound given by the HSV for the first 50 modes. The peak value for the Navier–Stokes system is 144.6 which is gradually approached by the ROM, until it saturates at a peak value of 144.5 due to numerical round-off errors. Note that the error is somewhat lower than the theoretical bounds for the reduced systems of orders 2 and 4. This is because the frequency response of the full system is obtained numerically using our timestepper and because $\|G\|_\infty$ is based on the maximum of the envelope of the TFM instead of its largest singular value.

A thorough comparison between the ROMs obtained with POD modes and balanced modes can be found in Ilak & Rowley (2008) for the case of channel flow and Bagheri *et al.* (2008) for the linear Ginzburg–Landau equation. The latter work also includes global eigenmodes of the linearized operator for comparison.

5. Feedback control

We will now develop a reduced-order feedback controller, which will have the same dimension as the ROM (e.g. $r = 50$). The closed-loop behaviour and the objective function z will be investigated and compared to the uncontrolled flat-plate boundary layer.

5.1. $\mathscr{H}_2$-*framework*

The main idea of linear feedback control is shown in figure 13. As stated in the introduction our objective is to find a control signal $u(t)$, such that in the presence of disturbances $w(t), g(t)$ the perturbation energy represented by the state variable $\boldsymbol{u}(\boldsymbol{x}, t)$ is minimized downstream at the location defined by the sensor $\mathscr{C}_1$. This is the $\mathscr{H}_2$ control problem.

In the previous section we showed that our reduced model (4.2) is able to capture the input-output behaviour of the Navier–Stokes system (2.12). During the control design process we can assume that the reduced model is the plant that we wish to control. Once we have determined the control law for this approximating model, we will apply it to the full Navier–Stokes system. Please refer to Anderson & Moore (1990), Zhou *et al.* (2002) and Bagheri *et al.* (2008) for further details of the $\mathscr{H}_2$ control algorithm, as we will only outline the main steps.

https://doi.org/10.1017/S0022112008004394 Published online by Cambridge University Press

Following the notation introduced for the reduced model (4.2), the objective function (2.11) becomes

$$\|z\|^2_{Y([0,\infty))} = \int_0^\infty q^T C_1^T C_1 q + l^2 u^T u \, \mathrm{d}\tau. \tag{5.1}$$

The determination of the control signal is based only on the measurements from the sensor $\mathscr{C}_2$. However, for linear systems – due to the separation principle (Zhou *et al.* 2002) – the feedback control law can be determined assuming that the complete velocity field is known. The forcing needed to reproduce the flow only from wall measurements can be computed independently. Hence, the control design of the $\mathscr{H}_2$ control is performed in the following three steps:

(i) Compute the control feedback gain K by solving a Riccati equation (see Appendix D), so that the control signal is of feedback type, i.e.

$$u(t) = Kq(t). \tag{5.2}$$

This leads to a new system (compared to (4.2)):

$$\dot{q} = (A + B_2 K)q + B_1 w, \tag{5.3a}$$

$$z = C_1 q. \tag{5.3b}$$

It is expected that the above perturbated operator $A + B_2K$ has dynamics that result in a smaller amplitude of the output signal z than for the unperturbated operator A in (4.2).

(ii) Compute the estimation feedback gain L also by solving a Riccati equation (see Appendix D), so that the observer

$$\dot{\hat{q}} = (A + LC_2)\hat{q} + Lv \tag{5.4a}$$

is asymptotically stable, i.e. $\|q - \hat{q}\| \to 0$ as $t \to \infty$. This implies that the estimated state $\hat{q}$ based on the measurements v approaches the true state q exponentially fast.

(iii) The compensator (controller in figure 13) is finally obtained as

$$\dot{\hat{q}} = (A + B_2K + LC_2)\hat{q} - Lv, \tag{5.5a}$$

$$u = K\hat{q}. \tag{5.5b}$$

Given the measurements signal v from the physical flow, the reduced-order controller provides an optimal control signal u proportional to the estimated flow $\hat{q}$.

To apply feedback control in the numerical simulations, an augmented state-space system with state $(\boldsymbol{u}, \hat{q})^T$ is considered: its dynamics are given by (2.12) and (5.5), inputs (w, g) and with the single output z:

$$\begin{pmatrix} \dot{\boldsymbol{u}} \\ \dot{\hat{q}} \end{pmatrix} = \begin{pmatrix} \mathscr{A} & \mathscr{B}_2 K \\ -L\mathscr{C}_2 & A + B_2K + LC_2 \end{pmatrix} \begin{pmatrix} \boldsymbol{u} \\ \hat{q} \end{pmatrix} + \begin{pmatrix} \mathscr{B}_1 & 0 \\ 0 & -L \end{pmatrix} \begin{pmatrix} w \\ g \end{pmatrix}, \tag{5.6a}$$

$$z = \mathscr{C}_1 \boldsymbol{u}. \tag{5.6b}$$

This system is referred to as the closed-loop system. Note that the feedback gain K and estimation gain L have the dimension of the reduced model, resulting in a fast online controller.

The spatio-temporal evolution of the perturbations governed by the closed-loop system is obtained by solving (5.6) numerically using the timestepper described in Appendix C and the small reduced system in (5.5) simultaneously. The latter system is solved using a standard Crank–Nicholson scheme.

https://doi.org/10.1017/S0022112008004394 Published online by Cambridge University Press

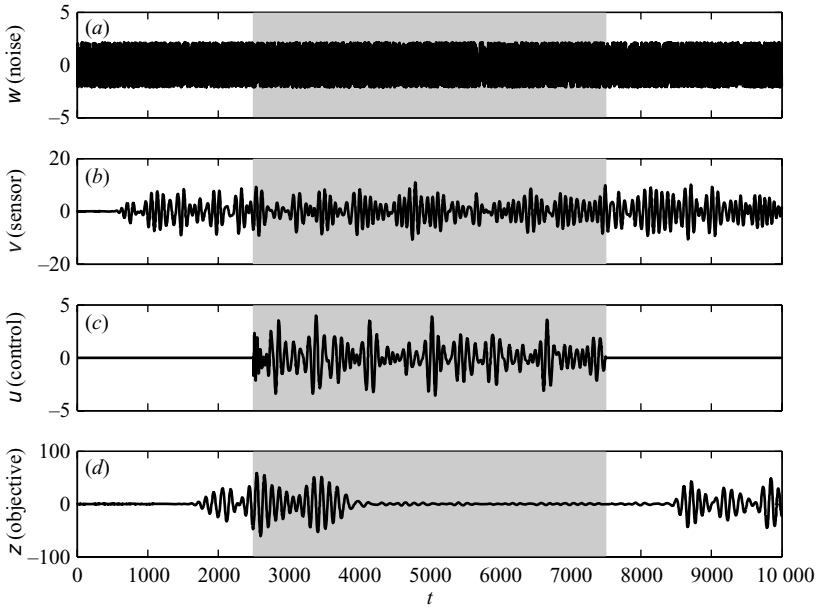


FIGURE 14. Input and output signals of the closed-loop system. The (*a*) random forcing w, (*b*) measurements signal v, (*c*) control signal u and (*d*) objective function z are shown. The cheap controller is active between $t \in [2500, 7500]$, represented by the grey area.

5.2. *Performance of closed-loop system*

We will now investigate the performance of the closed-loop system (5.6). In particular, the output z of the closed-loop – with optimal control signal u – and of the linearized Navier–Stokes equations without control are considered in the case of stochastic and harmonic forcings in w.

Three controllers are investigated: (i) cheap control/low noise contamination with $l = 0.1$ and $\alpha = 0.1$; (ii) expensive control/high noise contamination with $l = 10$ and $\alpha = 10$; and (iii) an intermediate case with $l = 2$ and $\alpha = 0.1$.

Note that the purpose of the measurement noise g is to account for uncertainties in the sensor measurements during the control design. When evaluating the closed-loop performance – solving the controlled Navier–Stokes equations – the system is only forced with w and not with g.

The performance of the control in case (i) is examined first. In figure 14 the input and output signals are shown. The grey region indicates the time at which the control is active. As disturbance signal $w(t)$ we choose white noise; the corresponding response of the sensor $v(t)$ in figure 14(*b*) confirms the amplification and filtering of the signal as it traverses the unstable domain. The disturbances reach the second sensor (figure 14*d*) after about 1500 time units, where they are amplified by one order of magnitude. The control is activated at time $t = 2500$; the actuator immediately begins to force the system with a control signal (figure 14*c*) based on the output v, and after a delay of another 1500 time units, the stabilizing effect of the control signal on the output z is clear. When the control is deactivated (at $t = 7500$) the disturbances start to grow again.

The wall normal maximum of the root mean square (r.m.s.) values of the streamwise velocity component in cases with and without control are shown in figure 15. The r.m.s. value grows exponentially downstream in the uncontrolled case until the fringe

https://doi.org/10.1017/S0022112008004394 Published online by Cambridge University Press

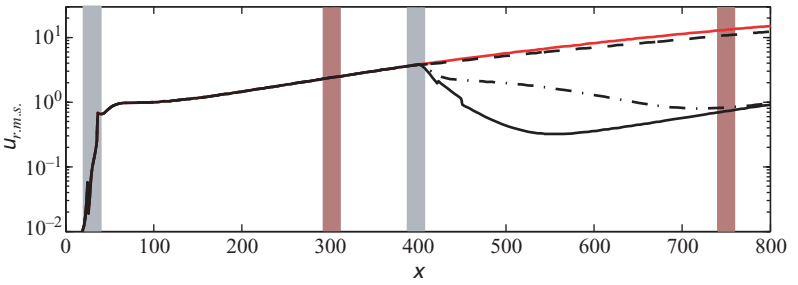


FIGURE 15. The r.m.s. values of the uncontrolled system (red line), cheap controller (solid black), intermediate controller (dashed–dotted line) and expensive controller (dashed line). The grey bar represent the size (defined as 99 % of the spatial support) and the location of the two inputs, whereas the red bars correspond to the two outputs.

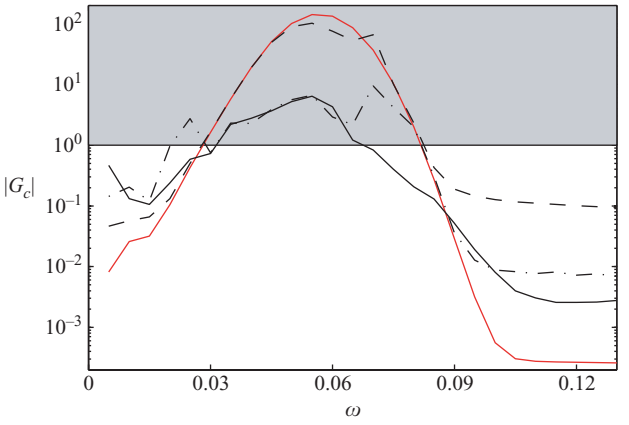


FIGURE 16. Comparison of the frequency response from disturbances to objective function ($\mathscr{B}_1 \rightarrow \mathscr{C}_1$) of open-loop (red) and three closed-loop systems. The cheap, intermediate and expensive controllers are represented by the solid black, dashed–dotted and dashed lines respectively. The infinity norm of the open loop is $\|G\|_\infty$ is 140.7, whereas for the closed-loop systems $\|G_c\|_\infty$ it is 6.4 (cheap), 9.4 (intermediate) and 101.9 (expensive).

region at $x = 800$. The r.m.s. of the controlled perturbation grows only until it reaches the actuator position at which it immediately begins to decay. At the location of the objective function $\mathscr{C}_1$ ($x = 750$), the amplitude of the perturbations is one order of magnitude smaller than in the uncontrolled case for the cheapest controller.

The r.m.s. values in the case of the expensive (case ii) and intermediate (case iii) controls are shown with dashed and dashed–dotted lines respectively. The expensive control is very conservative, as the measurement signals are highly corrupted and the control effort limited; it results only in a small damping of the disturbances. The intermediate controller (case iii) is more cautious in reducing the perturbation energy just downstream of the actuator when compared to the cheap controller. However, it is interesting to note that at the location at which the objective function is measured, the disturbance amplitude has decreased nearly as much as with the cheap controller, although the total perturbation energy is much larger over the entire domain.

In figure 16 the frequency response from $w \rightarrow z$ of the uncontrolled Navier–Stokes equations (2.12) (shown in red) is compared to that pertaining to the three controllers

https://doi.org/10.1017/S0022112008004394 Published online by Cambridge University Press

under consideration. The solid black line corresponds to cheap control, dashed–dotted line to intermediate control and dashed line to expensive control. The first two controllers suppress the most dangerous frequencies close to $\omega = 0.6$ significantly. Note that compared to the uncontrolled model, the highly damped frequencies $\omega > 0.11$ have larger gain in amplitudes. This behaviour is often observed in closed-loop physical systems and is related to the 'waterbed' effect; i.e. when certain frequencies are suppressed, the response at other frequencies is amplified.

6. Conclusions

Model-based feedback control of the instabilities arising in a spatially inhomogeneous boundary layer flow is studied. To build a reduced-order model of the problem, where the application of standard tools from control theory become computationally feasible also for fluid flow systems, the main features of the flow behaviour are investigated in an input-output framework. The observable, controllable and balanced modes of the system have been identified. The location and structure of these modes reflect the location of sensors/actuators and the perturbation dynamics; i.e the observable modes are located upstream, where the sensitivity to initial conditions is the largest. The controllable modes, conversely, are located downstream, where the response to the forcing is the largest. The analysis presented here can be closely related to stability analysis, using global modes and optimal disturbances, except that inputs and outputs are taken into account. The quantity one wishes to optimize for is now defined by a sensor output, while perturbations are introduced by the inputs considered in the model. Furthermore, in view of the control application, the formulation of the control objective function as an output is particularly attractive in this input-output setting, since this behaviour is well captured by the ROM.

Model reduction is achieved by projecting the governing equations on the leading balanced modes of the system. We show that the input-output behaviour of the flat-plate boundary layer can be captured accurately with an ROM based on these modes. Finally, the model is used to apply feedback control based on measurements from one upstream sensor and an actuator further downstream. The perturbations growth could be reduced efficiently using the $\mathscr{H}_2$ optimal feedback controller.

It is also important to note that the approach followed here requires only the use of a timestepper, a numerical code solving the Navier–Stokes equations, and avoids the use of the large matrices defining the operators governing the input-output behaviour. In addition, the present formulation accounts naturally for localized sensors and actuators, and therefore, it can be directly applied to different flow configurations. We are currently extending the analysis to three-dimensional disturbances and also incorporating more realistic actuators (blowing/suction) and sensors (wall measurements). These computations are now feasible and will take us a step closer to using the controller in actual experiments.

The authors would like to thank Professor Martin Berggren, Professor Gunilla Kreiss, Espen Åkervik, Milos Ilak, Antonios Monokrousos and Jonas Keissling for many interesting discussions. This work was partially sponsored by the Air Force Office of Scientific Research, through the European Office EOARD, under grant/contract number FA8655-07-1-3053. The authors also acknowledge the financial support from the Swedish Research Council (VR).

https://doi.org/10.1017/S0022112008004394 Published online by Cambridge University Press

Appendix A. Derivation of adjoint operators

A.1. *The adjoint operators $\mathscr{A}^*$, $\mathscr{B}^*$ and $\mathscr{C}^*$*

For a bounded linear operator between two Hilbert spaces, $\mathscr{L} : \mathbb{X}_1 \to \mathbb{X}_2$, the adjoint operator $\mathscr{L}^*$ satisfies

$$\langle \mathscr{L}\boldsymbol{q}, \boldsymbol{p}\rangle_{\mathbb{X}_2} = \langle \boldsymbol{q}, \mathscr{L}^*\boldsymbol{p}\rangle_{\mathbb{X}_1} \quad \text{for all} \quad \boldsymbol{q} \in \mathbb{X}_1, \boldsymbol{p} \in \mathbb{X}_2. \tag{A 1}$$

The derivations make use of the following definitions of inner products:

$$\left.\begin{aligned} \langle \boldsymbol{u}, \boldsymbol{p}\rangle_{\mathbb{X}} &= \int_\Omega \boldsymbol{u}(\boldsymbol{x})^T \boldsymbol{p}(\boldsymbol{x})\,\mathrm{d}x\,\mathrm{d}y, & \forall \boldsymbol{u}, \boldsymbol{p} \in \mathbb{X},\\ \langle \boldsymbol{f}, \boldsymbol{g}\rangle_{\mathbb{U}} &= \boldsymbol{f}^T\boldsymbol{g}, & \forall \boldsymbol{f}, \boldsymbol{g} \in \mathbb{U},\\ \langle \boldsymbol{z}, \boldsymbol{y}\rangle_{\mathbb{Y}} &= \boldsymbol{z}^T\boldsymbol{y}, & \forall \boldsymbol{z}, \boldsymbol{y} \in \mathbb{Y},\\ \langle \boldsymbol{f}, \boldsymbol{g}\rangle_{\mathbb{U}((-\infty,0])} &= \int_{-\infty}^{0} \boldsymbol{f}^T\boldsymbol{g}\,\mathrm{d}t, & \forall \boldsymbol{f}, \boldsymbol{g} \in \mathbb{U}((-\infty, 0]),\\ \langle \boldsymbol{z}, \boldsymbol{y}\rangle_{\mathbb{Y}([0,\infty))} &= \int_{0}^{\infty} \boldsymbol{z}^T\boldsymbol{y}\,\mathrm{d}t, & \forall \boldsymbol{z}, \boldsymbol{y} \in \mathbb{Y}([0, \infty)). \end{aligned}\right\} \tag{A 2}$$

Note that the kinetic energy of a perturbation $\boldsymbol{u}$ at time t is measured by $\|\boldsymbol{u}\|^2_{\mathbb{X}} = \langle \boldsymbol{u}, \boldsymbol{u}\rangle_{\mathbb{X}}$. We begin by deriving the adjoint operator of $\mathscr{B} : \mathbb{U} \to \mathbb{X}$, using the identity

$$\langle \mathscr{B}\boldsymbol{f}, \boldsymbol{u}\rangle_{\mathbb{X}} = \langle \boldsymbol{f}, \mathscr{B}^*\boldsymbol{u}\rangle_{\mathbb{U}}. \tag{A 3}$$

The left-hand side is equivalent to

$$\int_\Omega (\mathscr{B}\boldsymbol{f})^T\boldsymbol{u}\,\mathrm{d}x\,\mathrm{d}y = \boldsymbol{f}^T\int_\Omega \mathscr{B}^T\boldsymbol{u}\,\mathrm{d}x\,\mathrm{d}y = \langle \boldsymbol{f}, \int_\Omega \mathscr{B}^T\boldsymbol{u}\,\mathrm{d}x\,\mathrm{d}y\rangle_{\mathbb{U}}; \tag{A 4}$$

using (A 3) we identify $\mathscr{B}^* : \mathbb{X} \to \mathbb{U}$

$$\mathscr{B}^*\boldsymbol{u} = \int_\Omega \mathscr{B}^T\boldsymbol{u}\,\mathrm{d}x\,\mathrm{d}y. \tag{A 5}$$

The adjoint of the output operator $\mathscr{C} : \mathbb{X} \to \mathbb{Y}$ can be derived in an analogous manner by using the identity

$$\langle \mathscr{C}\boldsymbol{u}, \boldsymbol{y}\rangle_{\mathbb{Y}} = \langle \boldsymbol{u}, \mathscr{C}^*\boldsymbol{y}\rangle_{\mathbb{X}}. \tag{A 6}$$

The left-hand side can be written as

$$(\mathscr{C}\boldsymbol{u})^T\boldsymbol{y} = \int_\Omega \boldsymbol{u}^T\hat{\mathscr{C}}^T\boldsymbol{y} = \langle \boldsymbol{u}, \hat{\mathscr{C}}^T\boldsymbol{y}\rangle_{\mathbb{X}}, \tag{A 7}$$

where $\hat{\mathscr{C}}$ is the integrand in (2.17). We can now identify the adjoint output operator $\mathscr{C}^* : \mathbb{Y} \to \mathbb{X}$ as

$$\mathscr{C}^*\boldsymbol{y} = \hat{\mathscr{C}}^T\boldsymbol{y}. \tag{A 8}$$

The evolution operator $\mathscr{T} : \mathbb{X} \to \mathbb{X}$ has been defined in (2.4). The adjoint of $\mathscr{T}$ satisfies

$$\langle \mathscr{T}\boldsymbol{u}, \boldsymbol{p}\rangle_{\mathbb{X}} = \langle \boldsymbol{u}, \mathscr{T}^*\boldsymbol{p}\rangle_{\mathbb{X}}. \tag{A 9}$$

We begin with taking the inner product of $\boldsymbol{p}$ and σ with the Navier–Stokes equations (2.1*a*) and (2.1*b*), respectively. By integrating over the time domain and

https://doi.org/10.1017/S0022112008004394 Published online by Cambridge University Press

applying integration by parts we obtain

$$0 = \int_0^t \int_\Omega \left(\boldsymbol{p}^T \left[\frac{\partial \boldsymbol{u}}{\partial t} - (-(\boldsymbol{U}\cdot\nabla) - (\nabla \boldsymbol{U}^T)^T + Re^{-1}\nabla^2 + \lambda(x))\boldsymbol{u} - \nabla p \right] + \sigma(\nabla\cdot\boldsymbol{u}) \right) \mathrm{d}x\,\mathrm{d}y\,\mathrm{d}t$$
$$= \underbrace{\int_0^t \int_\Omega \left(-\boldsymbol{u}^T \left(\frac{\partial \boldsymbol{p}}{\partial t} + ((\boldsymbol{U}\cdot\nabla) - (\nabla \boldsymbol{U})^T + Re^{-1}\nabla^2 + \lambda(x))\boldsymbol{p} + \nabla\sigma \right) - p(\nabla\cdot\boldsymbol{p}) \right) \mathrm{d}x\,\mathrm{d}y\,\mathrm{d}t}_{1}$$
$$+ \underbrace{\int_0^t [B.C.]_\Omega \,\mathrm{d}t}_{2} + \underbrace{\int_\Omega \boldsymbol{u}(t)^T \boldsymbol{p}(t)\,\mathrm{d}x\,\mathrm{d}y - \int_\Omega \boldsymbol{u}(0)^T \boldsymbol{p}(0)\,\mathrm{d}x\,\mathrm{d}y}_{3} \tag{A 10}$$

By requiring the first two terms to be zero we obtain the adjoint Navier–Stokes equations with boundary conditions. They will be considered after the boundary terms in time denoted by 3 in (A 10). We thus require that

$$\int_\Omega \boldsymbol{u}(t)^T \boldsymbol{p}(t)\,\mathrm{d}x\,\mathrm{d}y = \int_\Omega \boldsymbol{u}(0)^T \boldsymbol{p}(0)\,\mathrm{d}x\,\mathrm{d}y. \tag{A 11}$$

The left-hand side can be rewritten as

$$\int_\Omega (\mathscr{T}(t)\boldsymbol{u}(0))^T \boldsymbol{p}(t)\,\mathrm{d}x\,\mathrm{d}y = \langle \mathscr{T}(t)\boldsymbol{u}(0),\, \boldsymbol{p}(t)\rangle_{\mathbb{X}}$$
$$= \langle \boldsymbol{u}(0), \mathscr{T}^*(t)\boldsymbol{p}(t)\rangle_{\mathbb{X}} = \int_\Omega \boldsymbol{u}(0)^T \mathscr{T}^*(t)\boldsymbol{p}(t)\,,$$

where we can identify the action of the adjoint evolution operator $\mathscr{T}^* : \mathbb{X} \to \mathbb{X}$ as

$$\mathscr{T}^*(t)\boldsymbol{p}(t) = \boldsymbol{p}(0). \tag{A 12}$$

Now we proceed with deriving the adjoint equations associated with $\mathscr{T}^*$. The spatial boundary terms given by the second term in (A 10) are

$$\int_0^t [B.C.]_\Omega \,\mathrm{d}t = \int_0^t \left[\sigma u + u^* p + U\boldsymbol{u}^T \boldsymbol{p} - Re^{-1}\boldsymbol{p}^T \frac{\partial \boldsymbol{u}}{\partial x} + Re^{-1}\boldsymbol{u}^T \frac{\partial \boldsymbol{p}}{\partial x} \right]_0^{L_x}$$
$$+ \left[\sigma v + v^* p + V\boldsymbol{u}^T \boldsymbol{p} - Re^{-1}\boldsymbol{p}^T \frac{\partial \boldsymbol{u}}{\partial y} + Re^{-1}\boldsymbol{u}^T \frac{\partial \boldsymbol{p}}{\partial y} \right]_0^{L_y} \mathrm{d}t = 0.$$

If boundary conditions (2.2) on $\boldsymbol{u}$ are used and if we demand that $\boldsymbol{p} = (u^*, v^*)$, σ^* and that p satisfy

$$(\sigma, p)(0, y) = (\sigma, p)(L_x, y), \tag{A 13a}$$
$$\boldsymbol{p}(0, y) = \boldsymbol{p}(L_x, y), \tag{A 13b}$$
$$\boldsymbol{p}(x, 0) = \boldsymbol{p}(x, L_y) = 0, \tag{A 13c}$$

we observe that the boundary terms vanish.

Finally, the first term in (A 10) defines the adjoint Navier–Stokes equations if we demand that $\boldsymbol{p}$ satisfy (2.23). Together with boundary conditions (A 13*b*) and (A 13*c*), (2.23) determine the behaviour of adjoint flow field $\boldsymbol{p}$.

A.2. *The adjoint operators $\mathscr{L}_c^*$ and $\mathscr{L}_o^*$*

The adjoint of the controllability operator $\mathscr{L}_c : \mathbb{U}((-\infty, 0]) \to \mathbb{X}$ is derived using the identity

$$\langle \mathscr{L}_c \boldsymbol{f}, \boldsymbol{u}_0\rangle_{\mathbb{X}} = \langle \boldsymbol{f}, \mathscr{L}_c^* \boldsymbol{u}_0\rangle_{\mathbb{U}((-\infty,0])}. \tag{A 14}$$

https://doi.org/10.1017/S0022112008004394 Published online by Cambridge University Press

We expand the left-hand side:

$$\begin{aligned}\langle \mathscr{L}_c \boldsymbol{f}, \boldsymbol{u}_0\rangle_{\mathbb{X}} &= \int_\Omega \int_{-\infty}^{0} (\mathscr{T}(-t)\mathscr{B}\boldsymbol{f}(t))^T \boldsymbol{u}_0 \,\mathrm{d}t\,\mathrm{d}x\,\mathrm{d}y \\ &= \int_{-\infty}^{0} \boldsymbol{f}^T(t)(\mathscr{B}^*\mathscr{T}^*(-t))\boldsymbol{u}_0 \,\mathrm{d}t \\ &= \langle \boldsymbol{f}(t), \mathscr{B}^*\mathscr{T}^*(-t)\boldsymbol{u}_0\rangle_{\mathbb{U}((-\infty,0])}.\end{aligned}$$

In the first equality the definitions of $\mathscr{B}^*$ and $\mathscr{T}^*$ from (A 5) and (A 9) were used. We can now identify $\mathscr{L}_c^* : \mathbb{X} \to \mathbb{U}((-\infty, 0])$

$$\mathscr{L}_c^*(-t)\boldsymbol{u}_0 = \mathscr{B}^*\mathscr{T}^*(-t)\boldsymbol{u}_0. \tag{A 15}$$

In a similar fashion the adjoint of the observability operator $\mathscr{L}_o : \mathbb{X} \to \mathbb{Y}([0, \infty))$ is defined by

$$\langle \mathscr{L}_o \boldsymbol{u}, \boldsymbol{y}\rangle_{\mathbb{Y}([0,\infty))} = \langle \boldsymbol{u}, \mathscr{L}_o^* \boldsymbol{y}\rangle_{\mathbb{X}}. \tag{A 16}$$

Expanding the left-hand side results in

$$\begin{aligned}\langle \mathscr{L}_o \boldsymbol{u}, \boldsymbol{y}\rangle_{\mathbb{Y}([0,\infty))} &= \int_0^\infty (\mathscr{C}\mathscr{T}(t)\boldsymbol{u}(t))^T \boldsymbol{y} \,\mathrm{d}t \\ &= \int_0^\infty \int_\Omega (\hat{\mathscr{C}}\mathscr{T}(t)\boldsymbol{u}(t))^T \boldsymbol{y} \,\mathrm{d}x\,\mathrm{d}y\,\mathrm{d}t \\ &= \int_0^\infty \int_\Omega \boldsymbol{u}^T (\mathscr{T}^*(t)\mathscr{C}^*\boldsymbol{y}(t))^T \,\mathrm{d}x\,\mathrm{d}y\,\mathrm{d}t \\ &= \left\langle \boldsymbol{u}, \int_0^\infty \mathscr{T}^*\mathscr{C}^*\boldsymbol{y}\,\mathrm{d}t \right\rangle_{\mathbb{X}},\end{aligned}$$

where $\hat{\mathscr{C}}$ is the integrand in (2.17). We can identify the adjoint observability operator $\mathscr{L}_o^* : \mathbb{Y}([0, \infty)) \to \mathbb{X}$ as

$$\mathscr{L}_o^* \boldsymbol{y}(t) = \int_0^\infty \mathscr{T}^*(t)\mathscr{C}^*\boldsymbol{y}(t)\,\mathrm{d}t. \tag{A 17}$$

Appendix B. The snapshot method

We will show how to approximate the eigenvalue problems (3.8), (3.4) and (3.18) in order to compute the observable, controllable and balanced modes.

B.1. *Approximate Gramians*

We begin with considering the eigenvalue problem

$$\mathscr{P}\boldsymbol{\phi}_i^c = \lambda_i^c \boldsymbol{\phi}_i^c, \tag{B 1}$$

where

$$\mathscr{P}\boldsymbol{\phi}_i^c = \int_0^\infty \mathscr{T}(t)\mathscr{B}\mathscr{B}^*\mathscr{T}^*(t)\boldsymbol{\phi}_i^c \,\mathrm{d}t. \tag{B 2}$$

The first step is to rewrite the action of the controllability Gramian $\mathscr{P}$ on $\boldsymbol{\phi}_i^c$ in terms of impulse responses of the state. Recall that the flow field triggered by an impulse $\delta(0)$ applied to the input $\mathscr{B}_1$ is given by $\mathscr{T}\mathscr{B}_1$. Let us define the vector $\bar{\boldsymbol{u}}$ containing the impulse responses of all inputs (except the measurement noise) as columns, i.e.

$$\bar{\boldsymbol{u}} = \mathscr{T}\mathscr{B} = (\mathscr{T}\mathscr{B}_1(\boldsymbol{x}), \mathscr{T}\mathscr{B}_2(\boldsymbol{x})) = (\boldsymbol{u}_1(\boldsymbol{x}, t), \boldsymbol{u}_2(\boldsymbol{x}, t)). \tag{B 3}$$

https://doi.org/10.1017/S0022112008004394 Published online by Cambridge University Press

Moreover, from the expression of $\mathscr{B}^*$ and $\mathscr{T}^*$ given by (A 5) and (A 9) respectively, we can rewrite the action of $\mathscr{B}^*\mathscr{T}^*$ on $\boldsymbol{\phi}_i^c$ as

$$\mathscr{B}^*\mathscr{T}^*\boldsymbol{\phi}_i^c = \int_\Omega (\mathscr{T}\mathscr{B})^T\boldsymbol{\phi}_i^c \,\mathrm{d}x\,\mathrm{d}y = \int_\Omega \bar{\boldsymbol{u}}^T\boldsymbol{\phi}_i^c \,\mathrm{d}x\,\mathrm{d}y. \tag{B 4}$$

The controllability Gramian becomes

$$\mathscr{P}\boldsymbol{\phi}_i^c = \left(\int_0^\infty \mathscr{T}(t)\mathscr{B}\mathscr{B}^*\mathscr{T}^*(t)\,\mathrm{d}t\right)\boldsymbol{\phi}_i^c = \int_0^\infty \bar{\boldsymbol{u}}\left(\int_\Omega \bar{\boldsymbol{u}}^T\boldsymbol{\phi}_i^c \,\mathrm{d}x\,\mathrm{d}y\right)\mathrm{d}t. \tag{B 5}$$

This expression is approximated by discretization in space and time. Suppose that $\boldsymbol{x} = (\boldsymbol{x}_1, \ldots, \boldsymbol{x}_{n/2})$ is a grid in Ω with $n/2$ points. We construct an $n \times 2$ matrix by evaluating $\bar{\boldsymbol{u}}$ at the grid points, i.e.

$$\hat{u} = \begin{pmatrix} \boldsymbol{u}_1(\boldsymbol{x}_1, t) & \boldsymbol{u}_2(\boldsymbol{x}_1, t) \\ \vdots, & \vdots \\ \boldsymbol{u}_1(\boldsymbol{x}_{n/2}, t) & \boldsymbol{u}_2(\boldsymbol{x}_{n/2}, t) \end{pmatrix}. \tag{B 6}$$

The size of this matrix is $n \times 2$ because it has two velocity components, e.g. $\boldsymbol{u}_1(\boldsymbol{x}_j, t) = (u_{1,1}, (\boldsymbol{x}_j, t), u_{1,2}(\boldsymbol{x}_j, t))^T$. Similarly we define $\hat{\phi}_i$ as the following $n \times 1$ column vector:

$$\hat{\phi}_i = \left(\boldsymbol{\phi}_i^c(\boldsymbol{x}_1), \ldots, \boldsymbol{\phi}_i^c(\boldsymbol{x}_{n/2})\right)^T. \tag{B 7}$$

The integral in Ω in (B 5) can now be approximated by

$$\int_\Omega \bar{\boldsymbol{u}}^T\boldsymbol{\phi}_i^c \,\mathrm{d}x\,\mathrm{d}y \approx \hat{u}^T W\hat{\phi}_i, \tag{B 8}$$

where the $n \times n$ positive-definite matrix W contains the spatial integration weights $\delta_{\boldsymbol{x}_j}$. The quadrature weights $\delta_{\boldsymbol{x}_j}$ depend on the chosen quadrature rule. For instance in our case, $\delta_{\boldsymbol{x}_j}$ consist of the Chebyshev integral weight functions (Hanifi, Schmid & Henningson 1996) in the wall normal direction and a trapezoidal rule in the streamwise direction.

The expression given by (B 5) becomes

$$\mathscr{P}\boldsymbol{\phi}_i^c \approx \left(\int_0^\infty \hat{u}\hat{u}^T\,\mathrm{d}t\right) W\hat{\phi}_i, \tag{B 9}$$

where we recognize the term in the parenthesis as the state-covariance matrix. If the flow fields are given as snapshots at discrete times $t_1, \ldots, t_m$, we can further approximate (B 9) with

$$\left(\int_0^\infty \hat{u}\hat{u}^T\,\mathrm{d}t\right) W\hat{\phi}_i \approx XX^T W\hat{\phi}_i. \tag{B 10}$$

The $n \times 2m$ matrix X contains $\hat{u}(t_j)$ in column j, multiplied with the square root of the quadrature coefficients δ_{t_j} in time, i.e.

$$X = (\hat{u}(t_1)\sqrt{\delta_{t_1}}, \ldots, \hat{u}(t_m)\sqrt{\delta_{t_m}}), \tag{B 11}$$

where each column of X is referred to as a snapshot.

The eigenvalue problem given by (B 1) can now be approximated with the following $n \times n$ eigenvalue problem:

$$XX^T W\hat{\phi}_i = \lambda_i^c\hat{\phi}_i, \qquad i = 1, \ldots, n. \tag{B 12}$$

https://doi.org/10.1017/S0022112008004394 Published online by Cambridge University Press

It is prohibitively expensive to diagonalize the matrix XX^TW when $n \geqslant 10^5$. In the method of snapshots (Sirovich 1987), the modes $\hat{\boldsymbol{\phi}}_i$ can be approximated by diagonalizing the $2m \times 2m$ matrix X^TWX instead. This is efficient when the product of the number of snapshots and the number of inputs is much smaller than the number of spatial grid points.

In the method of snapshots the modes $\hat{\boldsymbol{\phi}}_i$ are expanded in snapshots, i.e. the columns of matrix X. This can be formulated in matrix form as

$$\boldsymbol{\phi}_i^c = X\boldsymbol{a}_i, \qquad i = 1, \ldots, 2m, \tag{B 13}$$

with the column vector $\boldsymbol{a}_i$ containing the expansion coefficients.

The above expansion is inserted into the large eigenvalue problem (B 12), which results in the $2m \times 2m$ eigenvalue problem

$$X^TWX\boldsymbol{a}_i = \lambda_i^c\boldsymbol{a}_i, \qquad i = 1, \ldots, 2m. \tag{B 14}$$

The eigenvalues λ_i^c are the same as the original eigenvalue problem, and the controllable modes are recovered from (B 13). The orthonormal set of controllable modes are given by

$$\hat{\boldsymbol{\phi}}_i = \frac{1}{\sqrt{\lambda_i}}X\boldsymbol{a}_i, \qquad \hat{\boldsymbol{\phi}}_i^T\hat{\boldsymbol{\phi}}_j = \delta_{ij}. \tag{B 15}$$

There are some important computational issues which should now be commented at: (i) The Gramian 3.2 is defined as an infinite integral, which means that in order for the 'approximate' Gramian XX^TW to be a sufficiently good approximation, we should take snapshots for a long time. There are no restrictions on how to distribute the snapshots in time, and it is prudent to store many snapshots when the flow energy is large. (ii) Due to numerical round-off errors, often not all modes are orthogonal. In our case with $2m = 3200$, the first 150 modes were orthogonal down to numerical accuracy (i.e $(\boldsymbol{\phi}_i^c)^T\boldsymbol{\phi}_i^c \approx 10^{-15}$), whereas for higher modes the orthogonality condition was gradually lost due to rounding errors. The ratio $\mu_i = \lambda_1/\lambda_i$ can be used as a condition number of the corresponding mode $\boldsymbol{\phi}_i^c$. Very large values of μ_i indicate poor orthogonality due to numerical inaccuracy.

The observable modes are computed in a similar manner, but now the snapshots are taken from impulse responses of the adjoint equations for each output, i.e. $\bar{\boldsymbol{p}} = (\boldsymbol{p}_1, \boldsymbol{p}_2) = (\mathscr{T}^*\hat{\mathscr{C}}_1^T, \mathscr{T}^*\hat{\mathscr{C}}_2^T)$ with $\hat{\mathscr{C}}$ as the integrand in (2.17). The approximate observability Gramian is

$$\mathscr{Q}\boldsymbol{\phi}_i^o = \int_0^\infty \mathscr{T}^*\mathscr{C}^*\mathscr{C}\mathscr{T}\boldsymbol{\phi}_i^o \,\mathrm{d}t = \int_0^\infty \bar{\boldsymbol{p}}\left(\int_\Omega \bar{\boldsymbol{p}}^T\boldsymbol{\phi}_i^o \,\mathrm{d}x\,\mathrm{d}y\right)\mathrm{d}t \approx YY^TW\hat{\boldsymbol{\phi}}_i, \tag{B 16}$$

where Y is the $n \times 2m$ matrix:

$$Y = \begin{pmatrix} \boldsymbol{p}_1(\boldsymbol{x}_1, t_1)\sqrt{\delta_{t_1}} & \ldots & \boldsymbol{p}_1(\boldsymbol{x}_1, t_1)\sqrt{\delta_{t_1}} & \ldots & \boldsymbol{p}_2(x_1, t_m)\sqrt{\delta_{t_m}} \\ \vdots & & \vdots & & \vdots \\ \boldsymbol{p}_1(\boldsymbol{x}_{n/2}, t_1)\sqrt{\delta_{t_1}} & \ldots & \boldsymbol{p}_1(\boldsymbol{x}_{n/2}, t_1)\sqrt{\delta_{t_1}} & \ldots & \boldsymbol{p}_2(x_{n/2}, t_m)\sqrt{\delta_{t_m}} \end{pmatrix}. \tag{B 17}$$

The observable modes are computed in an analogous manner as the controllable modes with Y, replacing X in (B 13)–(B 15).

B.2. *Snapshot-based balanced truncation*

To obtain the balanced modes, we must diagonalize the matrix $\mathscr{P}\mathscr{Q}$, which can be approximated using the matrices X and Y, i.e.

$$\mathscr{P}\mathscr{Q}\boldsymbol{\phi}_i^{oc} \approx XX^TWYY^TW\hat{\boldsymbol{\phi}}_i^{oc} = \sigma_i^2\hat{\boldsymbol{\phi}}_i^{oc}. \tag{B 18}$$

https://doi.org/10.1017/S0022112008004394 Published online by Cambridge University Press

We expand the balanced modes as linear combinations of the columns of X, with $\boldsymbol{a}_i = (a_1, \ldots, a_m)^T$ as the expansion coefficients. Inserting this expansion in (B 18), we get

$$0 = XX^T WYY^T WX\boldsymbol{a}_i - X\boldsymbol{a}_i\sigma_i^2 = X\left(X^T WYY^T WX\boldsymbol{a}_i - \boldsymbol{a}_i\sigma_i^2\right). \tag{B 19}$$

To solve this problem we can equivalently diagonalize $X^T WYY^T WX$ or form the singular value decomposition (SVD) of $Y^T WX$. The latter decomposition is preferred, since it is numerically more stable, i.e.

$$Y^T WX\boldsymbol{b}_i = \sigma_i\boldsymbol{a}_i, \qquad i = 1, \ldots, 2m. \tag{B 20}$$

The normalized balanced modes and the associated adjoint balanced modes are recovered from

$$\hat{\phi}_i^{oc} = \frac{1}{\sqrt{\sigma_i}} X\boldsymbol{b}_i, \qquad \hat{\psi}_i^{oc} = \frac{1}{\sqrt{\sigma_i}} Y\boldsymbol{a}_i, \tag{B 21}$$

where $(\hat{\psi}_i^{oc})^T \hat{\phi}_j^{oc} = \delta_{ji}$.

The method can be summarized in three steps: (i) Compute the impulse response of each input; collect snapshots of the response; and construct X (B 11). (ii) Compute the adjoint impulse response of each output; collect snapshots of the response; and construct Y (B 17). (iii) Form the matrix $Y^T WX$; compute its SVD; and recover the balanced modes from (B 21). See Rowley (2005) for further details on the method.

Appendix C. Timestepper

The timestepper used in this work for both the forward and the adjoint equations is a spectral code described in detail in Chevalier *et al.* (2007*b*).

If $f(x, y, t)$ is a velocity component, then the discrete approximation is the Chebyshev-Fourier series

$$f(t) = \sum_{l=0}^{n_y} T_l(y) \sum_{m=-n_x/2}^{n_x/2} \mathrm{e}^{\mathrm{i}\alpha_m x} \hat{u}_{lm} + \text{c.c.}, \tag{C 1}$$

where T_l is the lth Chebyshev polynomial, $\alpha_m = 2m\pi/L_x$, and $n_x = 768$ and $n_y = 101$ the numbers of collocation points in each direction. The coefficients $\hat{u}_{lm}$ are complex functions. The associated collocation grid is defined by $y_l = (L_y/2)(1-\cos(\pi l/n_y))$ and $x_m = L_x(1/2 + m/n_x)$ with $L_x = 1000$ and $L_y = 30$. The discretized system of equations is projected onto a divergence-free space by transforming to v–η formulation and integrated in time using a third-order semi-implicit scheme.

To retain periodic boundary conditions, which is necessary for the Fourier discretization, a fringe region is added at the end of the physical domain in which a forcing is applied so that the flow smoothly changes from the outflow velocity of the physical domain to the desired inflow velocity. For the linearized equation the desired inflow condition is zero; so the fringe forcing is of the form $F = \lambda(x)\boldsymbol{u}$, where

$$\lambda(x) = -\lambda_{max}\left[S\left(\frac{x - x_{start}}{\Delta_{rise}}\right) - S\left(\frac{x - x_{end}}{\Delta_{fall}}\right)\right]. \tag{C 2}$$

Here λ_{max} is the maximum strength of the damping, $x_{start} = 800$ to $x_{end} = 1000$ the spatial extent of the region in which the damping function is non-zero and $\Delta_{rise} = 120$ and $\Delta_{fall} = 60$ the rise and fall distances of the damping function. The smooth 'step' function $S(x)$ rises from zero for negative x to one for $x \geqslant 1$. We have used the

https://doi.org/10.1017/S0022112008004394 Published online by Cambridge University Press

following form for S, which has the advantage of having continuous derivatives of all orders:

$$S(x) = \begin{cases} 0\,, & x \leqslant 0\,, \\ 1/\left(1 + \mathrm{e}^{(1/(x-1)+1/x)}\right), & 0 < x < 1\,, \\ 1\,, & x \geqslant 1\,. \end{cases} \tag{C 3}$$

Appendix D. Riccati equations

We briefly outline the full-information control and estimation problems and their solutions. The reader is directed to Anderson & Moore (1990), Lewis & Syrmos (1995) and Bagheri *et al.* (2008) for derivations of the solutions.

The first step in the design of an $\mathscr{H}_2$ compensator involves the solution of an optimal control state-feedback problem. The full-information problem is to find a control $u(t)$ as a linear function of the flow state $q(t)$ that minimizes the deterministic cost functional

$$J = \frac{1}{2}\int_0^\infty q^T C_1^T C_1 q + l^2 u^T u \,\mathrm{d}t \tag{D 1}$$

while satisfying the initial value problem

$$\dot{q} = Aq + B_2 u, \qquad q(t=0) = q_0. \tag{D 2}$$

The optimal control signal is given by

$$u(t) = \underbrace{-\frac{1}{l^2} B_2^T X}_{K} q(t), \tag{D 3}$$

where X is a solution of the Riccati equation

$$0 = A^T X + XA - \frac{1}{l^2} X B_2 B_2^T X + C_1^T C_1. \tag{D 4}$$

The solution to this equation provides the optimal steady feedback gain via the relation (D 3).

The second step in the design of an $\mathscr{H}_2$ compensator involves the minimization of the estimation error $q_e = q - \hat{q}$ given by the estimator

$$\dot{q}_e = Aq_e + B_1 w + L(v - \hat{v}), \qquad \hat{q}(t=0) = 0, \tag{D 5}$$

$$\hat{v} = C_1 \hat{q}, \tag{D 6}$$

$$v = C_1 q + g\,, \tag{D 7}$$

where w and g are temporal white noise signals. The solution is the feedback gain L that minimizes the objective functional

$$J = \int_0^\infty q_e^T(t) q_e(t)\,\mathrm{d}t. \tag{D 8}$$

The functional (D 8) can be minimized if L is chosen as

$$L = -\frac{1}{\alpha^2} P C_2^T, \tag{D 9}$$

where P is a solution of the Riccati equation

$$0 = AP + PA^T - \frac{1}{\alpha^2} P C_2^T C_2 P + B_1 B_1^T. \tag{D 10}$$

https://doi.org/10.1017/S0022112008004394 Published online by Cambridge University Press

REFERENCES

Ahuja, S., Rowley, C. W., Kevrekidis, I. G. & Wei, M. 2007 Low-dimensional models for control of leading-edge vortices: equilibria and linearized models. *AIAA Paper 2008-553, 46th AIAA Aeros. Sci. Meeting Exhibit*.

Åkervik, E., Ehrenstein, U., Gallaire, F. & Henningson, D. S. 2008 Global two-dimensional stability measures of the flat plate boundary-layer flow. *Eur. J. Mech.* B **27**, 501–513.

Åkervik, E., Hœpffner, J., Ehrenstein, U. & Henningson, D. S. 2007 Optimal growth, model reduction and control in a separated boundary-layer flow using global eigenmodes. *J. Fluid. Mech.* **579**, 305–314.

Anderson, B. & Moore, J. 1990 *Optimal control: Linear Quadratic Methods*. Prentice Hall.

Bagheri, S., Hœpffner, J., Schmid, P. & Henningson, D. 2009 Input-output analysis and control design applied to a linear model of spatially developing flows. *Appl. Mech. Rev.* In press.

Barkley, D., Gomes, M. G. & Henderson, R. D. 2002 Three-dimensional instability in flow over a backward-facing step. *J. Fluid Mech.* **473**, 167–190.

Bewley, T., Temam, R. & Ziane, M. 2000 A general framework for robust control in fluid mechanics. *Physica* D **138**, 360–392.

Blackburn, A. M., Barkley, D. & Sherwin, S. 2008 Convective instability and transient growth in flow over a backward-facing step. *J. Fluid Mech.* **603**, 271–304.

Butler, K. & Farrell, B. F. 1992 Three-dimensional optimal perturbations in viscous shear flow. *Phys. Fluids* A **4**, 1637–1650.

Chevalier, M., Hœpffner, J., Åkervik, E. & Henningson, D. S. 2007*a* Linear feedback control and estimation applied to instabilities in spatially developing boundary layers. *J. Fluid Mech.* **588**, 163–187.

Chevalier, M., Schlatter, P., Lundbladh, A. & D. S., H. 2007*b* A pseudo spectral solver for incompressible boundary layer flows. *Tech Rep.* 7. Trita-Mek, KTH Mechanics, Stockholm, Sweden.

Chomaz, J. M. 2005 Global instabilities in spatially developing flows: non-normality and nonlinearity. *Annu. Rev. Fluid Mech.* **37**, 357–392.

Chorin, A. & Marsden, J. 1990 *A Mathematical Introduction to Fluid Mechanics*. Springer.

Curtain, R. & Zwart, H. 1995 *An Introduction to Infinite-Dimensional Linear Systems Theory*. Springer.

Dullerud, E. & Paganini, F. 1999 *A Course in Robust Control Theory: A Convex Approach*. Springer.

Ehrenstein, U. & Gallaire, F. 2005 On two-dimensional temporal modes in spatially evolving open flows: the flat-plate boundary layer. *J. Fluid Mech.* **536**, 209–218.

Gillies, E. A. 1998 Low-dimensional control of the circular cylinder wake. *J. Fluid Mech.* **371**, 157–178.

Hanifi, A., Schmid, P. & Henningson, D. 1996 Transient growth in compressible boundary layer flow. *Phys. Fluids* **8** (3), 826–837.

Högberg, M., Bewley, T. R. & Henningson, D. S. 2003 Linear feedback control and estimation of transition in plane channel flow. *J. Fluid Mech.* **481**, 149–175.

Ilak, M. & Rowley, C. W. 2008 Modeling of transitional channel flow using balanced proper orthogonal decomposition. *Phys. Fluids* **20**, 034103.

Kailath, T. 1980 *Linear Systems*. Prentice-Hall.

Kim, J. & Bewley, T. R. 2007 A linear systems approach to flow control. *Annu. Rev. Fluid Mech.* **39**, 383–417.

Kreiss, G., Lundbladh, A. & Henningson, D. 1993 Bounds for threshold amplitudes in subcritical shear flows. *J. Fluid Mech.* **1994**, 175–198.

Lauga, E. & Bewley, T. R. 2003 The decay of stabilizability with reynolds number in a linear model of spatially developing flows. *Proc. R. Soc. Lond.* A **459**, 2077–2095.

Lewis, F. L. & Syrmos, L. V. 1995 *Optimal Control*. John Wiley.

Moore, B. 1981 Principal component analysis in linear systems: Controllability, observability, and model reduction. *IEEE Trans. Auto. Control* **26** (1), 17–32.

Noack, B., Afanasiev, K., Morzynski, M., Tadmor, G. & Thiele, F. 2003 A hierarchy of low-dimensional models for the transient and post-transient cylinder wake. *J. Fluid Mech.* **497**, 335–363.

https://doi.org/10.1017/S0022112008004394 Published online by Cambridge University Press

Nordström, J., Nordin, N. & Henningson, D. 1999 The fringe region technique and the fourier method used in the direct numerical simulation of spatially evolving viscous flows. *SIAM J. Sci. Comput.* **20** (4), 1365–1393.

Pazy, A. 1983 *Semigroup of Linear Operators and Applications to Partial Differential Equations*, 2nd ed. Springer.

Rempfer, D. & Fasel, H. 1994 Evolution of three-dimensional coheren structures in a flat-plate boundary layer. *J. Fluid. Mech.* **260**, 351–375.

Rowley, C. W. 2005 Model reduction for fluids using balanced proper orthogonal decomposition. *Intl J. Bifurc. Chaos* **15** (3), 997–1013.

Siegel, S. G., Seidel, J., Fagley, C., Luchtenburg, D. M., Cohen, K. & McLaughlin, T. 2008 Low dimensional modelling of a transient cylinder wake using double proper orthogonal decomposition. *J. Fluid Mech.* **610**, 1–42.

Sirovich, L. 1987 Turbulence and the dynamics of coherent structures. Part I–III. *Quart. Appl. Maths* **45**, 561–590.

Skogestad, S. & Postlethwaite, I. 2005 *Multivariable Feedback Control: Analysis to Design*, 2nd edn. Wiley.

Trefethen, L. & Embree, M. 2005 *Spectra and Pseudospectra: The Behavior of Nonnormal Matrices and Operators*. Princeton University Press.

Willcox, K. & Peraire, J. 2002 Balanced model reduction via the proper orthogonal decomposition. *AIAA J.* **40** (11), 2323–2330.

Zhou, K., Doyle, J. & Glover, K. 2002 *Robust and Optimal Control*. Prentice Hall.

Zhou, K., Salomon, G. & Wu, E. 1999 Balanced realization and model reduction for unstable systems. *Intl J. Robust Nonlinear Control* **9**, 183–198.

https://doi.org/10.1017/S0022112008004394 Published online by Cambridge University Press